Journal of Chemical&Engineering Data

Assessment and Ranking of Difluoromethane (R32) and Pentafluoroethane (R125) Interatomic Potentials Using Several Thermophysical and Transport Properties Across Multiple State Points

Barnabas Agbodekhe, Eliseo Marin-Rimoldi, Yong Zhang, Alexander W. Dowling, and Edward J. Maginn*

Cite This: https://doi.org/10.1021/acs.jced.3c00379 Read Online

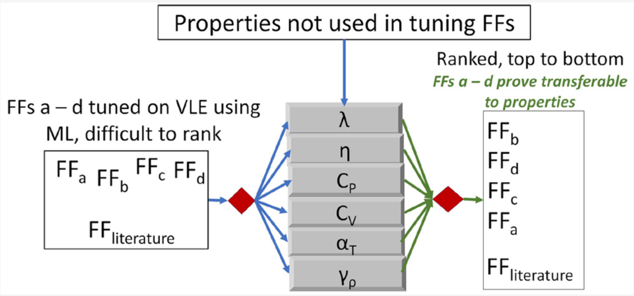

ABSTRACT: Difluoromethane (R32) and pentafluoroethane (R125) are two common hydrofluorocarbon refrigerants, often used in a mixture termed R410A. Many refrigerants, including R32 and especially R125, have high global warming potentials and so are being phased out. There is a desire to develop processes that can separate and recover these materials, which means that there is a need to determine the thermodynamic and transport properties of these fluids. In this work, we evaluate the ability of molecular dynamics simulations to determine the key thermodynamic and transport properties of these two fluids. We test whether classical interatomic force fields (FFs) parametrized against vapor−liquid equilibrium (VLE) data using a machine learning directed (MLD) approach can also yield accurate estimates of other key properties. The top-performing MLD FFs tuned against VLE data were nearly indistinguishable based on VLE results. This work seeks to investigate if these MLD-tuned FFs are transferable to other properties not used in tuning them and if they can be ranked to identify the "best" FFs. Literature FFs, one each for R32 and R125, are included in the study. A total of ten FFs were tested. Thermal conductivity (λ), viscosity (η), self-diffusivity (D), liquid density (ρ), isobaric heat capacity (C_P), isochoric heat capacity (C_V), thermal expansivity (α_P), thermal pressure coefficient (γ_ρ), isothermal compressibility (β_T), speed of sound (c_{sound}), Joule-Thomson coefficient (μ_{JT}), and center of mass radial distribution functions (g_r) were computed using molecular dynamics and compared with experiments when possible. Somewhat surprisingly, the MLD-tuned FFs are found to be transferable to a wide range of properties not used in tuning them. The MLD-tuned FFs were ranked. The FFs labeled $R32_a$ and $R125_b$ were found to be the "best" FFs for R32 and R125, respectively, across a broad range of properties. The MLD-tuned FFs were found to be superior to previously developed literature FFs.

■ INTRODUCTION

Hydrofluorocarbons (HFCs) are a class of materials that has been the focus of much research over the last several decades. This is due in part to the excellent suitability of HFCs as working fluids for heating, ventilation, air conditioning, and refrigeration (HVACR) systems with zero ozone depletion potential (ODP). They became popular due to phase out of chlorofluorocarbons (CFCs) and hydrochlorofluorocarbons (HCFCs), which were shown to be deleterious to the ozone layer.[1,2] HFCs are currently the major constituents of working fluid mixtures used in domestic, commercial, and industrial HVACR systems. They are also used in some fire extinguisher equipment and in the manufacturing of certain foam products as blowing agents.[3,4]

Unfortunately, HFCs have been found to contribute significantly to global warming due to their high global warming potentials (GWPs). The Kigali agreement has thus been signed by 197 countries to phase out the production and use of high GWP HFCs over the next few decades.[3−7] There are some technical challenges associated with the ongoing phaseout of HFCs. One of the challenges is to recover high GWP HFCs to prevent their continued release into the atmosphere through leaks and end-of-life disposal. Recovering harmful HFCs requires the design of efficient separation systems for refrigerant mixtures that are often azeotropic and difficult to separate.[8,9]

Special Issue: In Honor of Gabriele Sadowski

Received: June 20, 2023
Accepted: September 8, 2023

The task of predicting the thermodynamic and transport properties of HFCs can be achieved in a variety of ways. Equation of state (EoS)[10,11] and quantitative structure−property relationship (QSPR) methods[12−14] have been used mainly for obtaining pure component properties as well as properties of common refrigerant mixtures. However, the sustainable refrigeration challenge demands more than pure components or common refrigerant mixture properties. Future refrigeration systems will require the design of new refrigerant mixtures. These future refrigerant mixtures can be expected to be binary or even ternary mixtures of relatively low global warming potential (GWP) HFC molecules like difluoromethane (R32) and classes of molecules such as hydrofluoroolefins (HFOs), hydrochlorofluoroolefins (HCFOs), and other newer classes being discovered. Reliable experimental data on the thermodynamic and transport properties of binary and ternary mixtures of low GWP HFCs, HFOs, HCFOs, and other new refrigerant molecules are limited, and the combinatorial problem makes it challenging to measure all of the data needed. With scarce experimental data comes the consequence of limited EoS for these mixtures. Another area of need is in predicting the properties of mixtures of common refrigerant molecules and special materials like ionic liquids (ILs) for the separation and repurposing of, to be phased out, refrigerant mixtures. Yet another area of need is gaining a molecular-level understanding of the behavior of mixtures of older refrigerant molecules in solvents such as ILs as well as in future refrigerant mixtures. Molecular simulation (MS) naturally lends itself as the tool of choice for meeting these needs. Indeed, a synergy of diverse computational tools and expertise combined with experiments is needed to tackle the sustainable refrigerant problem.

MS has emerged as a valuable tool to predict thermodynamic and transport properties for materials of industrial interest and to understand their microscopic origin. MS can aid in the design of novel processes for challenging separations, such as those posed by HFC mixtures.[15−23] MS requires accurate representations of interatomic interactions to obtain reliable predictions of properties and elucidation of molecular-level phenomena. These representations, commonly referred to as force fields (FFs), are mathematical models that describe the potential energies and forces between interaction sites (usually atomic nuclei). FFs can be classified as class I, class II, or class III. Class I FFs use simple algebraic functional forms such as harmonic potentials, trigonometric functions, and the 12−6 Lennard-Jones potential to model bonds, torsional barriers, and dispersion interactions, respectively. They are widely used in the simulation community, in part because of their ease of implementation in MS software. Class II and class III FFs are more complicated FFs. They in general have functional forms that account for the coupling between neighboring bonds, angles, and dihedral angles. Class III FFs may also account for chemical effects as well as other features such as electronegativity and polarizability.[24,25] While most of the HFC force fields are class I FFs, a significant amount of work has also been devoted to developing these generally more complex classes of FFs for HFCs.[26−32] The present work focuses on testing and ranking class I FFs for difluoromethane (R32) and pentafluoroethane (R125). The primary rationale for the focus on class I FFs is due to their much better compatibility with available MS codes. Furthermore, molecular simulations with class I FFs can be expected to be faster than those using class II and class III FFs, resulting in significant savings in computational resources. Due to the relative simplicity of class I FFs, they are easier to develop and parametrize. One of the goals of this work is to see whether simple class I FFs are accurate for HFCs or if more sophisticated models are needed. Finally, for most practical applications and as will be further established in this work, well-parametrized class I FFs are adequate for capturing a broad range of the desired properties and molecular-level physics of relatively simple molecules like HFCs. It should be noted that the scope of the work presented in this manuscript is for all-atom, fully flexible models. Fully rigid, united atom models[33] are not within the scope of this manuscript and are, more importantly, not fit for our future intended purposes.

Generalized FFs, such as the General Amber Force Field (GAFF)[34] or the Optimized Potentials for Liquid Simulations All-Atom (OPLS-AA)[35] force field, provide parameters to generate class I force fields for a variety of small organic molecules, including HFCs. GAFF has parameters for many of the HFCs of interest, including the molecules of interest in this study, R32 and R125. The performance of the GAFF force field to simulate vapor−liquid equilibria (VLE) of R32 and R125 has been evaluated by Befort et al.[36] The authors showed that properties such as liquid and vapor densities were not well predicted. The limited accuracy of generalized FFs such as GAFF is, in part, the reason for much of the work that has gone into the development of molecule-specific FFs for these HFCs.

For example, Raabe[37] developed a fully flexible all-atom FF for R32 that was optimized to reproduce VLE properties. It was shown to give satisfactory predictions for saturated liquid density (ρ^{l}) and vapor density (ρ^{v}), enthalpy of vaporization (ΔH_{vap}), critical temperature (T_c), and critical pressure (P_c).[36,37] Fermeglia et al.[38] developed a class I FF for R125 using liquid density and VLE data for FF validation. The developed FFs were reported to show an excellent match with experimental VLE data. However, the FF parameters for R125 were unfortunately not published, and attempts to obtain the parameters from the authors failed.

Befort et al.[36] optimized FFs for R32 and R125 using an automated machine learning directed (MLD) method. The authors refined the GAFF Lennard-Jones parameters to develop R32 and R125 FFs that reproduce VLE properties[36] with high accuracy. The proposed MLD method produced twenty-six and forty-five distinct FF parameter sets for R32 and R125, respectively, that outperformed the best available FFs.[37] Recently, Wang et al.[39] applied this machine learning-driven FF optimization procedure to five other refrigerants: R143a, R134a, R50, R-170, and R-14. Other molecule-specific FFs for HFCs include R134a,[40] R152a,[41] and R161.[42] The aforementioned FFs were tuned to match specific thermodynamic properties, such as VLE. Only a limited number of additional properties have been computed with these force fields, leaving questions about their transferability to a wider range of properties and thermodynamic states.

The work presented in this paper seeks to extend the work of Befort et al.[36] by evaluating the transferability of their top-performing R32 and R125 models to other properties. Eleven thermophysical, transport, and structural properties not included in the FF tuning process, namely, thermal conductivity (λ), viscosity (η), self-diffusivity (D), isobaric heat capacity (C_P), isochoric heat capacity (C_V), thermal expansivity (α_P), thermal pressure coefficient (γ_ρ), isothermal compressibility (β_T), speed of sound (c_{sound}), Joule-Thomson

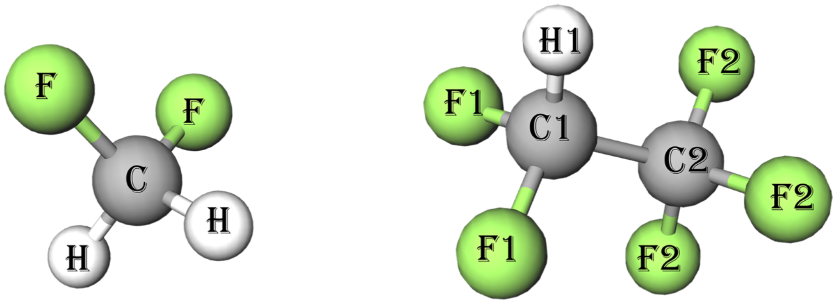

Figure 1. Molecular structures of R32 (left) and R125 (right) with atom type definitions.

Table 1. Bonded FF Parameters of R125 and R32 Taken from GAFF and the Derived Partial Charges Used in This Work

partial charges			
atom	GAFF atom type		q/(e)
C	c3		0.405467
F	f		−0.250783
H	h2		0.0480495
C1	c3		0.224067
C2	c3		0.500886
F1	f		−0.167131
F2	f		−0.170758
H1	h2		0.121583
bond type	k_r/(kJ·mol^{-1}·Å^{-2})		r_o/(Å)
c3-f	1493.3		1.3497
c3-h2	1387.8		1.0961
c3-c3	1259.0		1.5375
angle type	k_θ/(kJ·mol^{-1}·rad^{-2})		θ_o/(deg)
f-c3-f	296.6		107.36
f-c3-h2	213.8		108.79
c3-c3-f	276.6		109.24
c3-c3-h2	193.3		110.22
h2-c3-h2	163.2		110.20
dihedral type	ν_n/(kJ·mol^{-1})	n	γ/(deg)
f-c3-c3-f	5.02	1	180.0
f-c3-c3-h2	0.65	3	0.0

coefficient (μ_{JT}) and center of mass radial distribution functions (g_r), were computed. The simulations were conducted at several thermodynamic state points to further assess the transferability of the models. We include in this study the hand-tuned FF for R32 developed by Raabe[37] and the GAFF FF[34] for R125 used in the work by Befort et al.[36] We also evaluate the top four FFs for R32 and R125 developed by Befort et al.[36] These FFs could not be differentiated based on their performance in VLE calculations. One of our goals is to see whether the addition of other properties allows us to see differences in the performance of the different FFs. Another goal is to see if FFs parametrized against VLE data using machine learning methods can be used to obtain other properties with good accuracy. This work provides the most comprehensive set of molecular simulation FF validation data for these two important refrigerant fluids to date. This will serve as a foundation for future similar benchmarks for other HFCs and refrigerant molecules. Finally, this work provides a compilation of good practices on how to accurately compute the aforementioned properties, along with sample simulation setup and postprocessing scripts used in performing these calculations.

■ METHODS

Force Fields. Figure 1 presents the structure and atom types defined in this work for refrigerant molecules R32 and R125, respectively.

The functional form of all force fields used in this work is the same as that of GAFF.[34] Table 1 shows the bonded FF parameters from GAFF[34] version 1.40 and the partial charges derived previously[36] using the restrained electrostatic potential (RESP) method[43] for both R125 and R32. The parameters of the Raabe FF for R32 can be found elsewhere.[37] This FF is termed R32$_{Raabe}$ in this work. Note that R32$_{Raabe}$ parameters are completely different from all the MLD-tuned FFs for R32, whereas the only differences among the MLD-tuned FFs are in the LJ parameters for both R32 and R125. The R125 FF from GAFF differs from the MLD-tuned FFs for R125 only in terms of the LJ parameters.

Table 2 shows all of the FFs studied in this work and their LJ parameters. They include the top four MLD-tuned FFs for R125 and R32.[36] The parameter sets are labeled *a*, *b*, *c*, and *d*, respectively. The LJ parameters for R125 from GAFF[34] and those for R32 from Raabe[37] are also shown. This table stands in lieu of a chemical compounds and models table. Note that the atom type defined in this work for R125 is not the same as those used by GAFF. The corresponding GAFF atom types to those used in this work are presented in Table 1.

Simulation Details. All simulations were performed using the LAMMPS (June 23 2022 version)[44] molecular dynamics (MD) package. Initial box configurations were generated using PACKMOL[45,46] by randomly inserting 2000 (R32) or 1000 (R125) molecules in a cubic box. This was followed by an energy minimization scheme that applied the Polak−Ribiere version of the conjugate gradient algorithm as implemented in LAMMPS.[44] Initial velocities were assigned to the atoms from a Gaussian distribution such that there was no net angular or linear momentum in the simulation box. The resulting simulation box was then used for MD simulations in the isothermal−isobaric (NPT) ensemble. The final configurations at the equilibrium densities from the NPT simulations were used for corresponding simulations in the canonical (NVT) and microcanonical (NVE) ensembles. Simulations were performed in the NPT, NVT, and NVE ensembles to determine properties at saturated liquid conditions at temperatures of 243.15, 258.15, 273.15, and 298.15K and at pressures close to the corresponding saturated liquid pressures from the National Institute of Standards and Technology (NIST) chemistry webbook.[47]

A 12 Å cutoff distance for the LJ and electrostatic interactions was used for all simulations. Long-range tail

Table 2. LJ Parameters Studied in This Work[a]

	$\mathrm{R125}_a$	$\mathbf{R125}_b$	$\mathrm{R125}_c$	$\mathrm{R125}_d$	$\mathrm{R125}_{GAFF}$
			$\epsilon/k_B/(\mathrm{K})$		
C1	59.3807	**45.0463**	59.5321	43.0749	55.0522
C2	27.4944	**50.4590**	48.5607	52.4979	55.0522
F1	28.3145	**31.6841**	24.4512	20.3573	30.6964
F2	17.6325	**28.9380**	17.6264	23.3728	30.6964
H1	6.4942	**6.5283**	6.5810	9.7908	7.9005
			$\sigma/(\mathrm{Å})$		
C1	3.8049	**3.6946**	3.6614	3.1102	3.3997
C2	3.6167	**3.1003**	3.4576	3.9294	3.3997
F1	3.2009	**2.5192**	3.4845	2.7069	3.1181
F2	2.6441	**3.1586**	2.5062	3.1018	3.1181
H1	2.4877	**2.3889**	2.5833	2.4840	2.2932
	$\mathbf{R32}_a$	$\mathrm{R32}_b$	$\mathrm{R32}_c$	$\mathrm{R32}_d$	$\mathrm{R32}_{Raabe}$
			$\epsilon/k_B/(\mathrm{K})$		
C	**55.6481**	59.2086	59.5493	58.9345	54.6000
F	**39.1405**	30.0647	28.8311	38.8941	44.0000
H	**3.6644**	7.7619	9.3946	2.2268	7.9000
			$\sigma/(\mathrm{Å})$		
C	**3.7992**	3.7122	3.7096	3.6530	3.1500
F	**2.7427**	2.7555	2.8215	2.8658	2.9400
H	**1.9689**	2.2664	2.1281	1.9171	2.2930

[a] The ones with the best overall performance found in this work for R32 and R125 are indicated in bold.

Table 3. NPT Simulation Temperatures and Pressures for R32 and R125[a]

R32		R125	
$P/(\mathrm{kPa})$	$T/(\mathrm{K})$	$P/(\mathrm{kPa})$	$T/(\mathrm{K})$
271.41	**243.15**	**227.25**	**243.15**
	233.15		233.15
	223.15		223.15
488.58	**258.15**	**405.17**	**258.15**
	243.15		243.15
	233.15		233.15
807.28	**273.15**	**667.54**	**273.15**
	263.15		263.15
	258.15		258.15
	248.15		248.15
	243.15		243.15
1690.14	**298.15**	**1378.27**	**298.15**
	273.15		273.15
	263.15		263.15
	258.15		258.15
2479.13	298.15	2009.60	298.15
	273.15		273.15
3521.36.	298.15	2840.82	298.15

[a] The bold-faced temperatures are the saturation temperatures at which all computed properties are reported at the corresponding near-saturation pressures also in bold.

corrections were applied to the LJ interactions, and the Ewald summation method with a relative error in force computation of 0.0001 was used to handle long-range electrostatic interactions.[48,49] Periodic boundary conditions were applied in all directions of the orthogonal simulation boxes. Lorentz–Berthelot[50] combining rules were used to compute LJ interaction parameters between all unlike atoms. Thermostating and barostating were achieved using Nosé-Hoover style thermostatting and barostating schemes as implemented in LAMMPS.[44] The relaxation times for the thermostat and barostat were set to 100 and 1000 fs, respectively, for all NPT simulations. NVT simulations had only Nosé-Hoover style thermostatting with a relaxation time of 100 fs. The equations of motion developed by Shinoda et al.[51] were solved using the time integration algorithms that closely follow those developed by Tuckerman et al.[52] as implemented in LAMMPS[44] with a time step of 1.0 fs. Flexible bonds and angles were used in the current study, whereas they were fixed in previous work.[36]

NPT Simulations. NPT simulations were performed to calculate the residual isobaric heat capacity C_P^{res} and the thermal expansion coefficient α_p. One way to compute these thermodynamic quantities is to fit enthalpies and densities as a function of temperature. Table 3 shows the temperatures and corresponding pressures at which NPT simulations were performed to obtain the data for these fits. The selected thermodynamic state points correspond to either near-saturated or subcooled liquid states. For reference, the temperatures in bold correspond to near-saturated liquid conditions for the given pressures. Once the system had been prepared in the desired liquid state, NPT simulations were run for 15 ns. A code to automate the determination of the point of equilibration was used for all simulations and is available within the sample NPT postprocessing tools on the GitHub repository for this work at https://github.com/MaginnGroup/Validation-of-HFC-FFs. The point of equilibration ranged from 6.5 to 12 ns for R32 and from 6 to 10.5 ns for R125 after the system preparation, which involved an annealing scheme. Further details on the system preparation for NPT simulations are provided in the Supporting Information (SI). The simulation beyond the equilibration point was considered production and was used to compute average system properties such as density, configurational and internal energies, and enthalpies.

NVT Simulations. NVT simulations were performed to calculate the residual isochoric heat capacity C_V^{res} and the thermal pressure coefficient γ_ρ. Table 4 shows the temperatures and corresponding densities at which the NVT simulations were performed. ρ_t^* in Table 4 means the saturated liquid density obtained from NPT simulations at a temperature of t + 0.15 K. Final simulation box configurations from NPT

Table 4. NVT Simulation Temperatures and Densities for R32 and R125

$T/(\mathrm{K})$	$\rho_t^*/(\mathrm{kg{\cdot}m^{-3}})$
243.15	ρ_{243}^*
	$1.025 \times \rho_{243}^*$
	$1.05 \times \rho_{243}^*$
258.15	ρ_{258}^*
	ρ_{243}^*
	$1.025 \times \rho_{243}^*$
273.15	ρ_{273}^*
	ρ_{258}^*
	ρ_{243}^*
283.15	ρ_{273}^*
	ρ_{258}^*
298.15	ρ_{298}^*
	ρ_{273}^*
	$1.025 \times \rho_{273}^*$
313.15	ρ_{298}^*
323.15	ρ_{298}^*

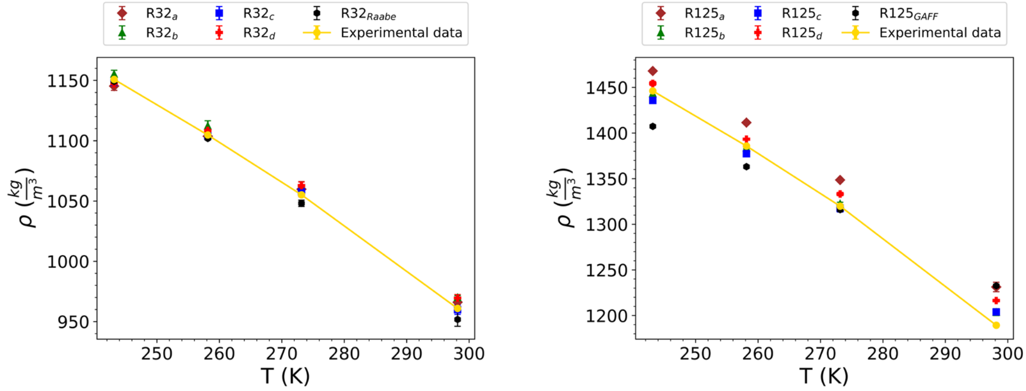

Figure 2. Density as a function of saturation temperature at the corresponding saturation pressure shown in Table 3 for R32 and R125. MAPEs are $R32_a$ = 0.39%, $R32_b$ = 0.63%, $R32_c$ = **0.16%**, $R32_d$ = 0.57%, and $R32_{Raabe}$ = 0.51%; $R125_a$ = 2.26%, $R125_b$ = **0.44%**, $R125_c$ = 0.68%, $R125_d$ = 1.10%, and $R125_{GAFF}$ = 2.06%.

simulations were used to start corresponding NVT simulations at the same temperature but with the densities adjusted to the desired simulation box densities, as shown in Table 4. It is important to note that the actual values of the densities in Table 4 are FF dependent for both R125 and R32. NVT simulation runs were performed for 15 ns, and the point of equilibration was determined as was done for NPT simulations. Postequilibration data were used in computing the average pressures and average configurational internal energies.

Choice of State Points Studied. We recognize that the complete fluid state regions for the HFCs studied include the gas, subcooled liquid, near-saturated liquid, VLE, and supercritical states. Studies on the models' ability to capture VLE properties have been completed in previous work.[36] The fluid state points in Tables 3 and 4 for which simulations were performed include the subcooled liquid and near-saturated liquid states. A total of 30 state points are included in Tables 3 and 4 at which simulations were performed. These state points include 4 near-saturated liquid state points and 26 subcooled liquid state points. We consider that the fluid state regions covered in this work in addition to the VLE region covered in previous work[36] represent the most important fluid state regions for these HFC applications in refrigeration. Certain gas phase properties, such as the gas phase heat capacity and compressibility, are important. It may be useful to investigate and benchmark these for our models in future studies. For the sake of completeness, the supercritical region may also be of interest in future studies.

General Uncertainty Quantification. The block averaging method by Flyvbjerg and Petersen[53,54] was used to estimate uncertainties of properties that were computed directly by simulation. The errors in derived thermodynamic properties, such as speed of sound (c_{sound}) or Joule-Thomson coefficient (μ_{JT}), were estimated by using error propagation formulas. Finally, the curve fitting tool in the optimize subpackage of the SciPy package[55] was used to estimate the error in properties that require linear fits, such as residual isobaric heat capacity. Additional details are available in the SI.

■ RESULTS AND DISCUSSION

Except where otherwise stated, all experimental data referred to in this work are taken from the NIST chemistry webbook and REFPROP.[47] Note that REFPROP results are actually derived from accurate models fit to the experimental data. These include the Tillner-Roth and Yokozeki's equation of state for R32 and Lemmon and Jacobsen's equation of state for R125.[10,11] It is generally accepted that REFPROP results, which apply to pure fluids and their mixtures, are valid over the entire fluid range, including gas, liquid, and supercritical states. It is claimed[47] that uncertainties approach the level of the underlying experimental data. We note that the equation of state (EoS) used in the NIST REFPROP calculations may not extrapolate quite well outside the temperatures at which experimental data were measured. The experimental data used in developing the EoS do cover, and actually go well beyond, the fluid state conditions for which we have used them in this work. In this work, we are assuming that the data from NIST REFPROP are reliable and reasonably sufficient for our purpose.

Numerical data presented in plots are available in tabular format in the SI of this work. In the plot captions, the percentage values represent the calculated mean absolute percentage errors (MAPEs) between simulation and experiments. All values in bold represent the minimum MAPEs for R32 and R125, respectively.

Density. Figure 2 shows the densities of R32 and R125 as a function of temperature for all of the FFs tested in this work. All FFs for R32 agree well with experiments across all temperatures studied. The MLD-tuned FFs for R125 have an excellent performance in capturing the density with temperature, although larger deviations from experimental values at higher temperatures are observed. The $R32_{Raabe}$ FF compares favorably with the MLD-tuned FF in capturing the liquid density for R32, whereas the GAFF FF for R125 shows generally worse performance compared with the MLD-tuned FFs.

Isobaric and Isochoric Heat Capacity. To calculate heat capacity, the ideal and residual contributions were computed according to the method described by Cadena et al.[56]

$$C_P = C_P^{ideal} + C_P^{res}, \quad C_V = C_V^{ideal} + C_V^{res} \tag{1}$$

The ideal parts were determined by quantum mechanical calculations. It would be possible to use tabulated ideal gas heat capacities for C_P^{ideal}, but we wanted to assess the accuracy of a fully computational approach. According to the recommendations by Lucas et al.,[57] the second-order Møller-Plesset perturbation theory (MP2) was applied to compute the molecular electronic energies with the 6-31G** basis set. All

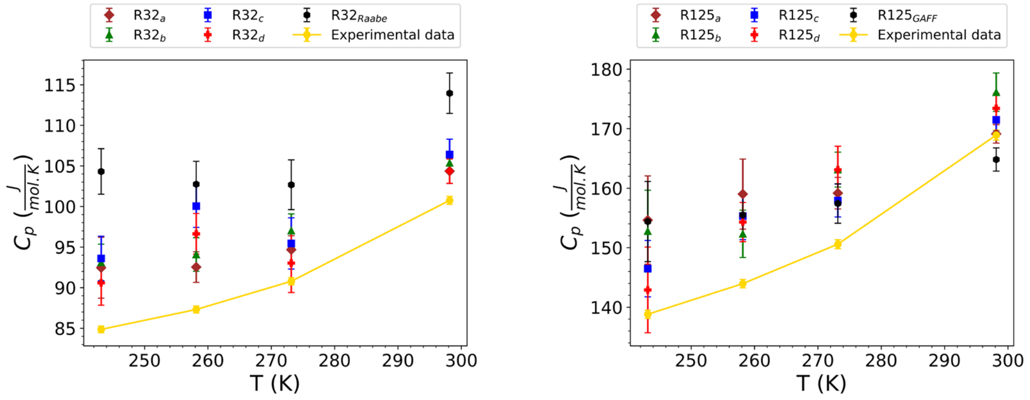

Figure 3. Isobaric heat capacity as a function of saturation temperature at the corresponding saturation pressure shown in Table 3 for R32 and R125. MAPEs are $R32_a$ = **5.70** %, $R32_b$ = 7.23%, $R32_c$ = 8.90%, $R32_d$ = 5.87%, and $R32_{Raabe}$ = 16.70%; $R125_a$ = 6.91%, $R125_b$ = 7.11%, $R125_c$ = **4.95** %, $R125_d$ = 5.27%, and $R125_{GAFF}$ = 6.55%.

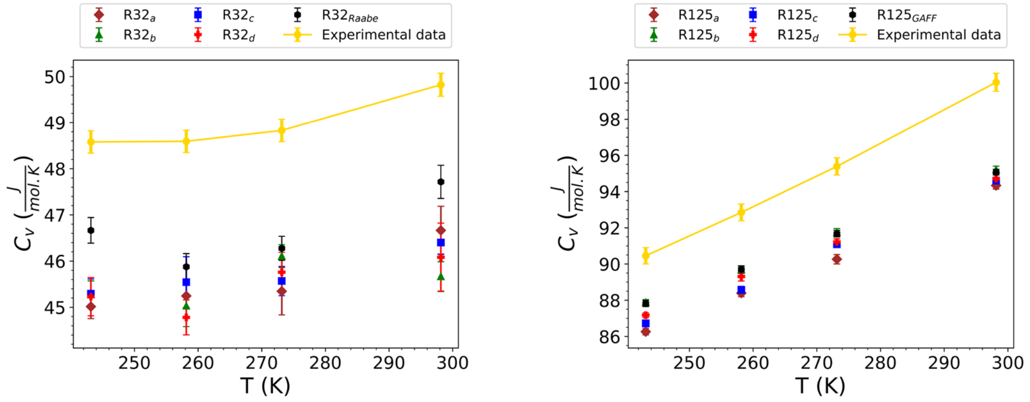

Figure 4. Isochoric heat capacity as a function of saturation temperature at the corresponding saturation pressure shown in Table 3 for R32 and R125. MAPEs are $R32_a$ = 6.92%, $R32_b$ = 7.01%, $R32_c$ = 6.64%, $R32_d$ = 7.13%, and $R32_{Raabe}$ = **4.75** %; $R125_a$ = 5.13%, $R125_b$ = **3.72** %, $R125_c$ = 4.67%, $R125_d$ = 4.28%, and $R125_{GAFF}$ = 3.79%.

quantum mechanical calculations were performed using the Psi4 package.[58] Values of the ideal isobaric and isochoric heat capacities, C_P^{ideal} and C_V^{ideal} of R125 and R32 were obtained with a 1−2% underestimation when compared with ideal heat capacities from NIST.[47] The residual portions of the isobaric and isochoric heat capacities C_P^{res} and C_V^{res} were computed from NPT and NVT simulations, respectively, according to eqs 2, 3, and 4.

$$C_P^{res} = \left(\frac{\partial H^{config}}{\partial T}\right)_P, \quad C_V^{res} = \left(\frac{\partial U^{config}}{\partial T}\right)_V \tag{2}$$

$$U^{config} = U_{intermol}^{vdwl} + U_{intermol}^{coul} + U^{long} \tag{3}$$

$$H^{config} = U^{config} + PV \tag{4}$$

where U^{config} and H^{config} are the configurational internal energy and enthalpy, respectively; they do not contain contributions from the kinetic and intramolecular energies.[59] $U_{intermol}^{vdwl}$ is the intermolecular van der Waals energy, $U_{intermol}^{coul}$ is the energy from intermolecular short-range Coulombic interactions within the electrostatic interaction cutoff, and U^{long} is the energy from long-range electrostatic interactions which are computed using the Ewald summation method[48] as implemented in LAMMPS.[44] $U_{intermol}^{vdwl}$ and $U_{intermol}^{coul}$ are not readily available from the output of a simulation. The *tally* package in recent versions of LAMMPS[44] was used to split the short-range Coulombic and van der Waals interactions into intramolecular and intermolecular components.

U^{config} and H^{config} were computed as described above, and the uncertainties were estimated accordingly. These quantities and their associated uncertainties were then fitted to temperature over a temperature range for which these quantities can be assumed to be linear with temperature. For the residual isobaric heat capacity at 243.15 K, the configurational enthalpies at 243.15, 233.15, and 223.15 K at a constant saturation pressure corresponding to 243.15 K were used. In a like manner, the value at 258.15 K was computed using configurational enthalpies at 258.15, 243.15, and 233.15 K. For 273.15 K, configurational enthalpies at 273.15, 263.15, and 248.15 K were used. Finally, configurational enthalpies at 298.15, 273.15, and 263.15 K at a fixed pressure corresponding to the saturation pressure at 298.15 K were used for computing the residual isobaric heat capacity at 298.15 K. These simulated state points are shown in Table 3. For the residual isochoric heat capacity at 243.15 K, the configurational internal energies at 243.15, 258.15, and 273.15 K at a constant saturated liquid density corresponding to 243.15 K were used. In a like manner, the value at 258.15 K was computed using configurational internal energies at 258.15, 273.15, and 283.15 K. For 273.15 K, configurational internal energies at 273.15, 283.15, and 298.15 K were used. Finally, configurational internal energies at 298.15, 313.15, and 323.15 K at a fixed saturated liquid density corresponding to 298.15 K were used for computing the residual isochoric heat capacity at 298.15 K. These simulated state points are detailed in Table 4. This allows the partial derivatives in eq 2 to be approximated using linear fits. The slope of these linear fits gives the residual isobaric or isochoric heat capacity. Note that the uncertainties from QM calculations are ignored, as they make negligible contributions. We also note that C_P^{res} and C_V^{res} can also be computed via appropriate fluctuation formulas. However, the use of the fluctuation equations has been reported to suffer from high statistical uncertainties.[56,60]

Figures 3 and 4 display the calculated isobaric and isochoric heat capacities for R32 and R125, respectively. The error bars in Figure 3 by visual observation may look large. However, a quantitative assessment of the relative magnitudes of these error bars using the relative standard deviations (RSDs), expressed in percentage form, shows that the maximum RSDs in the isobaric heat capacity results are 4.1% and 5.0% for R32 and R125, respectively. The minimum RSDs are 1.1% and 0.9%, respectively. These values are reasonably low, considering typical uncertainty values associated with this property in the context of a molecular simulation. Table S2 shows the values of the standard deviations associated with each computation of the isobaric heat capacity.

The MD results agree well with experiments in predicting the increasing trend in C_P and C_V with temperature, although some of the FFs for R32 show inconsistency between adjacent state points like 243.15 and 258.15 K as an example. Considering the uncertainties, MD simulations predict no difference between these close state points. A small systematic overestimation of C_P and underestimation of C_V is observed in general. However, the quantitative agreement between MD simulations and experiments is generally good for both C_P and C_V, especially given the difficulty of computing these "derivative" properties; errors are generally less than 10%. The MLD-tuned FFs generally perform better than the generalized GAFF FF for both C_P and C_V, and the expert-tuned FFs perform better for C_P. However, R32$_{Raabe}$ performed better than all of the R32 MLD-tuned FFs for C_V.

Thermal Expansion Coefficient (α_P). The thermal expansion coefficient α_P is given by eq 5. One way to apply this equation is to calculate the partial derivative $\left(\frac{\partial\rho}{\partial T}\right)_P$ using finite difference formulas. In practice, these finite difference methods are implemented by fitting ρ or lnρ data to a linear function of temperature at constant pressure in the temperature range that α_P is to be calculated.[61−63]

$$\alpha_P = -\frac{1}{\rho}\left(\frac{\partial\rho}{\partial T}\right)_P \tag{5}$$

In this work, we fitted ρ data from MD to a cubic function of both the pressure and temperature. This is a modification to the more common approach of doing a linear fit of ρ with temperature, as stated previously. The linear fit method assumes that ρ is a linear function of T at any given P and that the partial derivative of ρ with respect to T at a given P must be a constant value. These assumptions, although sometimes good enough, are not very accurate. A study of any EoS that relates ρ with T and P clearly shows that ρ is not a linear function of T and P. Applying a cubic fit to widely separated data from MD may allow a better representation of the relationship between ρ, T, and P over the entire T and P range of interest. In addition, the simple mathematical form of the cubic function allows for easy calculation of the required derivatives with a reasonable number of fitting parameters for the MD data used.

Equation 6 shows the cubic function used, while eq 7 is the corresponding expression for $\left(\frac{\partial\rho}{\partial T}\right)_P$. The values of the coefficients a_0 to a_9 in eq 6 are determined by fitting the ρ data obtained from NPT MD simulations at the conditions detailed in Table 3. With the coefficients determined, $\left(\frac{\partial\rho}{\partial T}\right)_P$ can then be evaluated according to eq 7 and α_P can then finally be computed using eq 5.

$$\rho = a_0 + a_1T + a_2P + a_3T^2 + a_4P^2 + a_5TP + a_6T^3 + a_7P^3 + a_8TP^2 + a_9T^2P \tag{6}$$

$$\left(\frac{\partial\rho}{\partial T}\right)_P = a_1 + 2a_3T + a_5P + 3a_6T^2 + a_8P^2 + 2a_9PT \tag{7}$$

The uncertainties in the values of α_P were estimated by using the block averaging method. Three blocks were considered, which ensured that the individual block sizes were large enough to minimize the correlation between them and to provide a sufficient number of separately computed values for calculating averages and uncertainties for α_P. We divided the last 3 ns of the postequilibration data for the instantaneous densities from molecular simulations into three blocks. We then found the average density of each block. Therefore, for each state point at which a simulation was performed, we had three values of computed average densities corresponding to the three blocks. This then meant we had three sets of average density values, corresponding to the three blocks, across all the state points, where, as an example, density values for the first block across all the state points at which simulations were performed correspond to the first set of density data and so on. We then independently used each of the three sets of density data to compute α_P at the desired saturation temperatures and pressures using the cubic fit method described above. This means that, for each saturation temperature and pressure of interest, we computed three values of α_P using the three sets of density data corresponding to the three blocks. The uncertainties (or error bars) correspond to the standard deviation of the three independently computed values of α_P for each saturation temperature and pressure of interest.

As is the case for C_P^{res} and C_V^{res}, α_P can also be computed via appropriate fluctuation formulas. However, calculations using these formulas may suffer from high statistical uncertainties.[56,60] The experimental values of α_P were indirectly obtained using eq 8, where $\langle V\rangle$ is the molar volume.

$$\alpha_P = \sqrt{\left((C_P - C_V)\frac{\beta_T}{T\langle V\rangle}\right)} \tag{8}$$

Experimental values of β_T, the isothermal compressibility, in eq 8 were obtained by using eq 9. The rest of the experimental data used in eqs 8 and 9 were obtained from the NIST REFPROP database.[47] c_{sound} is the speed of sound.

$$\beta_T = \frac{C_P}{{c_{sound}}^2 C_V\rho} \tag{9}$$

This indirect approach of obtaining the experimental values of α_P and also β_T by using standard thermodynamic

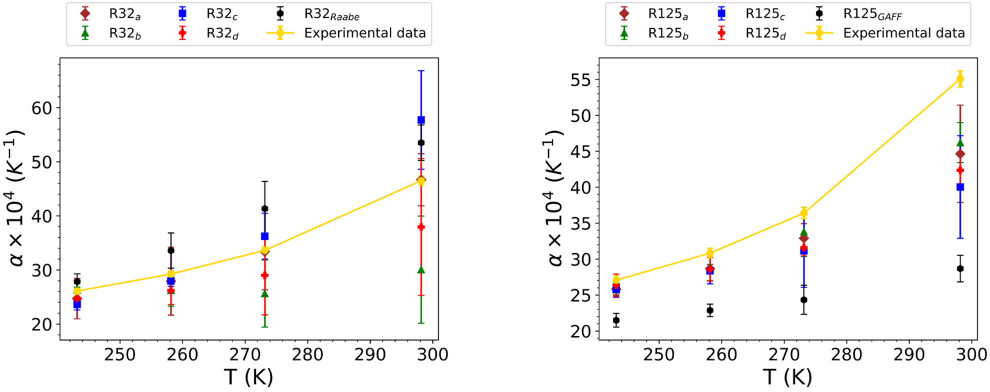

Figure 5. Thermal expansion coefficient as a function of saturation temperature at the corresponding saturation pressure shown in Table 3 for R32 and R125. MAPEs are R32$_a$ = **2.72** %, R32$_b$ = 17.57%, R32$_c$ = 11.42%, R32$_d$ = 11.95%, and R32$_{Raabe}$ = 14.89%; R125$_a$ = 10.04%, R125$_b$ = **8.59** %, R125$_c$ = 13.61%, R125$_d$ = 11.55%, and R125$_{GAFF}$ = 31.87%.

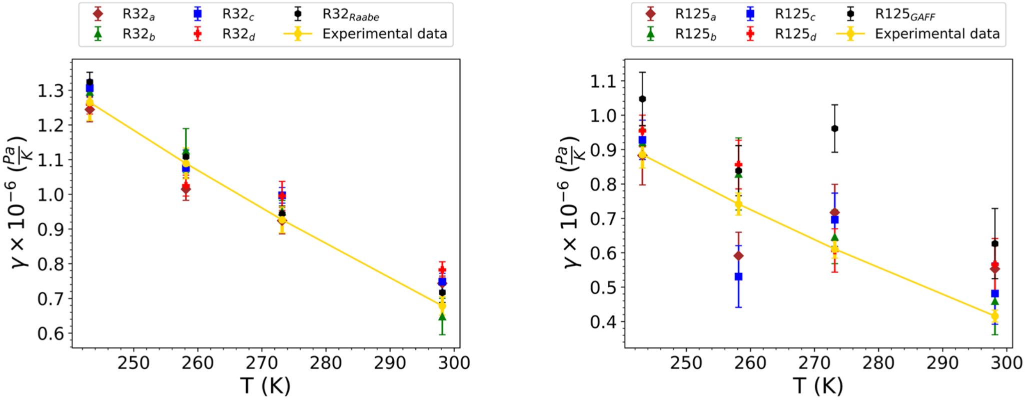

Figure 6. Thermal pressure coefficient as a function of saturation temperature at the corresponding saturation pressure shown in Table 3 for R32 and R125. MAPEs are R32$_a$ = 4.56%, R32$_b$ = **3.21** %, R32$_c$ = 5.59%, R32$_d$ = 7.24%, and R32$_{Raabe}$ = 3.47%; R125$_a$ = 17.75%, R125$_b$ = **8.02** %, R125$_c$ = 15.75%, R125$_d$ = 15.03%, and R125$_{GAFF}$ = 34.88%.

relationships was adopted to enable uncertainty quantification for these properties. The errors associated with these derivative properties were not readily or directly available via the NIST REFPROP database.[47]

Figure 5 shows α_P as a function of saturation temperature at corresponding saturation pressure shown in Table 3 for R32 and R125.

The general qualitative trends are well captured by the FFs for both R32 and R125. However, the quantitative agreement seems to be better at lower temperatures. Visual inspection of the error bars in Figure 5 may suggest that they are quite large. RSDs for α_P from molecular simulations are often in the range of 5−15%.[64−67] Uncertainties with higher RSDs than these have also been reported.[66,68] We confirm that the RSDs for most (about 75%) of the data points across multiple state points and models for α_P are well within the range of RSDs for α_P from some other molecular simulation studies. Most of the RSDs are between 2% and 15% for R32 and R125. The few data points that have higher relative uncertainties outside this range still have RSDs that are still comparable to some previous molecular simulation studies.[66,68] In any case, the relatively high uncertainties for these few data points do not undermine the overall comparisons in predictive performance between the models that are to be made for the case of α_P. In general, quantities with smaller magnitudes can be more challenging to capture precisely, resulting in higher relative uncertainties compared to some other properties.

It is important to state at this point that the general performance of these FFs for calculating α_P is impressive. α_P is a derivative property with numerically small values and is not always an easy property to compute within a 10% or even 20% accuracy based on results for similar calculations in the literature.[62,63,69] Alkhwaji et al.[69] computed α_P for water at multiple state points and obtained results that had a MAPE of approximately 20% relative to experiments. This MAPE was estimated by us from the plots of results for α_P as a function of temperature in the work by Alkhwaji et al.[69] They reported that the results were good enough for engineering applications. Wang et al.[62] obtained a mean percentage deviation of 21.7% from the experimental value in α_P at a single state point for an ionic liquid using different mole fractions of the constituent anions and cations. It was reported that this result was in good enough agreement with the experiments. All of the MLD-tuned FFs in this work and R32$_{Raabe}$ were able to predict α_P to less than 20% MAPE from experiments. Seven of the eight MLD-tuned FFs achieved less than 15% MAPE, with the best of them being able to capture this property to within 10% MAPE relative to experiments for both R32 and R125.

Thermal Pressure Coefficient (γ_ρ). The thermal pressure coefficient (γ_ρ) can be expressed as

$$\gamma_\rho = \left(\frac{\partial P}{\partial T}\right)_\rho \tag{10}$$

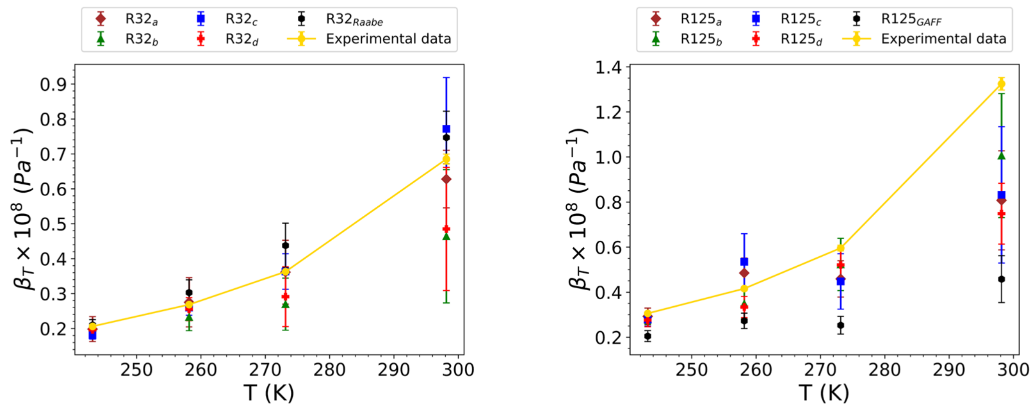

Figure 7. Isothermal compressibility as a function of saturation temperature at the corresponding saturation pressure shown in Table 3 for R32 and R125. MAPEs are R32$_a$ = **3.76** %, R32$_b$ = 18.16%, R32$_c$ = 7.06%, R32$_d$ = 14.65%, and R32$_{Raabe}$ = 11.12%; R125$_a$ = 20.75%, R125$_b$ = **15.24** %, R125$_c$ = 24.96%, R125$_d$ = 21.37%, and R125$_{GAFF}$ = 47.57%.

γ_ρ can also be defined according to

$$\gamma_\rho = \frac{\alpha_P}{\beta_T} \tag{11}$$

which was used in determining the experimental values of γ_ρ with uncertainties obtained using standard error propagation.

NVT simulations were performed under the conditions detailed in Table 4. Pressure data from MD were fitted to linear functions of temperature to approximate eq 10. Block averaging was used to determine the average pressure and uncertainties. The partial derivative in eq 10 was approximated using a linear fit of the pressure to temperature at a constant density. The uncertainties in the slopes of the linear fits were determined as previously discussed.

Figure 6 gives the plots of γ_ρ as a function of saturation temperature at the corresponding saturation pressure shown in Table 3 for R32 and R125. A good qualitative and quantitative agreement was observed for all R32 FFs with the lowest MAPE obtained being 3.21% for R32$_b$. The expert-tuned FF, R32$_{Raabe}$, compares favorably with the MLD-tuned FF for this property. The performance of the R125 FFs is worse when compared with the R32 FFs; however, the results are still reasonable. R125$_b$ and R125$_d$ excellently capture the qualitative trend in γ_ρ of a nearly linear decrease with increasing temperature. Other R125 FFs predict the overall trend but to a lesser degree of satisfaction. For example, between 258.15 and 273.15 K, the trend is contrary to experimental results. It is probable that there may be an underestimation in the uncertainties in the γ_ρ estimated for these two state points. This may arise from an underestimation of the uncertainties in the pressures by using block averaging. There may also be an underestimation of the uncertainties in the slopes of the linear fit of the pressure with temperature. As is well-known, instantaneous pressures from MD simulations show wide and erratic fluctuations. Thus, calculations using average pressures and errors in these averages can show the behavior observed in Figure 6 for some of the R125 FFs. R125$_b$ gives the best quantitative agreement with experiments with a MAPE of 8.02%. The MLD-tuned FFs generally perform better than the general FF R125$_{GAFF}$ for γ_ρ.

Isothermal Compressibility (β_T), Speed of Sound (c_{sound}), and Joule-Thomson Coefficient (μ_{JT}). The isothermal compressibility (β_T) can be computed using γ_ρ and α_P obtained from molecular simulation by rearranging eq 11 to give

$$\beta_T = \frac{\alpha_P}{\gamma_\rho} \tag{12}$$

with uncertainties estimated using error propagation. Experimental values of β_T were obtained using eq 9 as previously discussed.

This quantity can also be computed directly from a molecular simulation in either the isothermal−isobaric ensemble or the canonical ensemble according to the following expression

$$\beta_T = \frac{1}{\rho}\left(\frac{\partial \rho}{\partial P}\right)_T \tag{13}$$

using the finite-difference approach to approximate the partial derivatives.

It is evident that there are several routes to compute the set of thermodynamic properties investigated in this study. Our focus is not to assess the various routes but instead to use a route that is convenient and reliable. In general, of the three quantities α_P, γ_ρ, and β_T, only two need to be directly computed using MS. Once the choice of which two are to be directly computed is made, the third one can be indirectly computed using an appropriate form of eq 12. In this work, we chose to compute α_P and γ_ρ directly from MS as these quantities are significantly larger in magnitude than β_T. We opine that accurately computing derivative quantities such as β_T, which have very little magnitude, on the order of 10^{-8} Pa^{-1}, may be more challenging in general compared to γ_ρ, with magnitude on the order of 10^6 Pa·K^{-1}, when using the finite difference based methods.

Figure 7 shows that the FFs generally capture the qualitative trends of the increase in β_T with temperature. A decrease in β_T is observed between 258.15 and 273.15 K for some of the R125 FFs. This can be related to the behavior of the γ_ρ values between these two temperatures for the same FFs. As this property was indirectly computed, the quantitative accuracy, as well as uncertainties in this property, is a function of the accuracy and uncertainties in α_P and γ_ρ. This explains the large uncertainties associated with these values. Overall, R32$_a$ and R125$_b$ give the best quantitative agreement among the R32 and R125 FFs with a MAPE of 3.75% and 15.74% respectively,

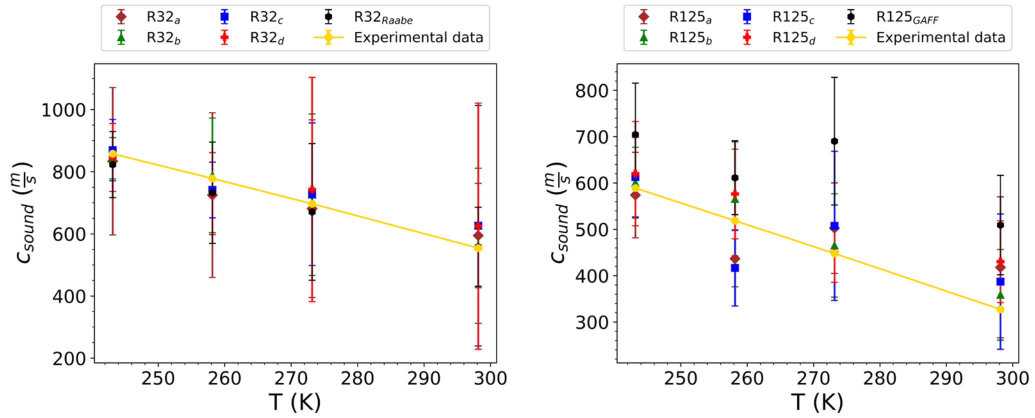

Figure 8. Speed of sound as a function of saturation temperature at the corresponding saturation pressure shown in Table 3 for R32 and R125. MAPEs are R32$_a$ = 4.82%, R32$_b$ = **2.11** %, R32$_c$ = 5.88%, R32$_d$ = 6.74%, and R32$_{Raabe}$ = 3.63%; R125$_a$ = 14.56%, R125$_b$ = **6.11** %, R125$_c$ = 13.80%, R125$_d$ = 12.08%, and R125$_{GAFF}$ = 36.77%.

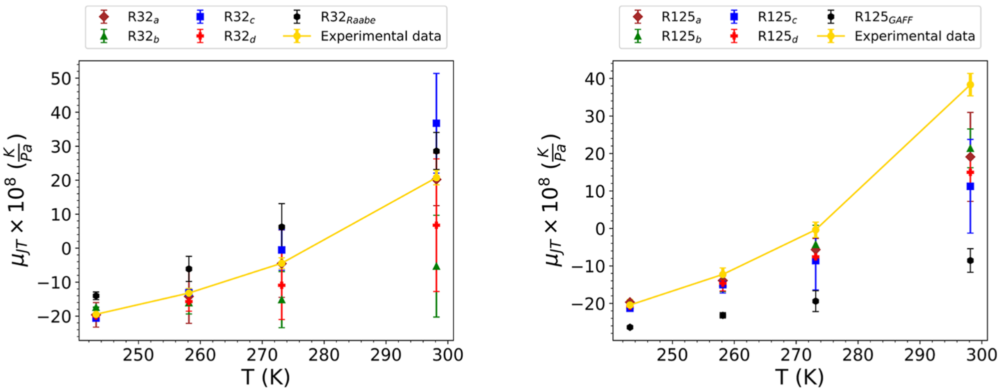

Figure 9. Joule-Thomson coefficient as a function of saturation temperature at the corresponding saturation pressure shown in Table 3 for R32 and R125. MAPEs are R32$_a$ = **3.44** %, R32$_b$ = 99.80%, R32$_c$ = 42.80%, R32$_d$ = 58.89%, and R32$_{Raabe}$ = 90.00%; R125$_a$ = 386.26%, R125$_b$ = **288.41** %, R125$_c$ = 598.58%, R125$_d$ = 523.89%, and R125$_{GAFF}$ = 1387.13%.

which can be considered a good agreement for a derivative property such as isothermal compressibility.

The speed of sound (c_{sound}) values were computed from other properties obtained via molecular simulation via the following expressions

$$c_{\mathrm{sound}}^{\ 2} = \frac{C_\mathrm{P}}{C_\mathrm{V}\beta_\mathrm{T}\rho} \tag{14}$$

$$C_\mathrm{V} = C_\mathrm{P} - \frac{T\langle V\rangle\alpha_\mathrm{P}^{\ 2}}{\beta_\mathrm{T}} \tag{15}$$

and standard error propagation was used to estimate uncertainties.

Values of C_P and C_V obtained as previously discussed could be used directly in eq 14. This was found to give less reliable results since the values of C_P and C_V systematically overestimate and underestimate experimental values, respectively, as previously stated and as shown in Figures 3 and 4. One approach for mitigating the effects of the errors in the individual properties to be used in calculating c_{sound} is to substitute for C_V in eq 14 by using eq 15. This is the approach adopted in this work and is the same approach used in the work by Aimoli et al.[59] An alternative approach is to substitute for C_P in eq 14 using eq 15 by expressing C_P in terms of C_V and other quantities in eq 15.

Figure 8 gives the calculated speed of sound of R32 and R125 as a function of temperature. The general qualitative trends are well captured. Again some of the FFs for R125 show an opposite trend as compared to experiments between 258.15 and 273.15 K. This again is due to the behavior observed for γ_ρ at these temperatures. The minimum MAPE values are 2.11% and 6.10% for R32 and R125, respectively, which is considered excellent for this property. R125$_{GAFF}$ gives a less satisfactory performance for this property.

Simulation and experimental values of the Joule-Thomson coefficient (μ_JT) were indirectly calculated using the following expression

$$\mu_\mathrm{JT} = \frac{\langle V\rangle(T\alpha_\mathrm{P} - 1)}{C_\mathrm{P}} \tag{16}$$

The uncertainties in μ_JT were computed by applying standard error propagation methods to eq 16.

Figure 9 shows the results of the computed μ_JT as a function of saturation temperature at the corresponding saturation pressure shown in Table 3 for R32 and R125. Visual observation of these plots shows qualitative agreement between simulation and experiments. However, a closer inspection suggests that the uncertainties in these values are extremely high as are the MAPE values, especially for R125. An analysis of eq 16 helps to understand, to some extent, why this is the case. It can easily be verified that the computed values of

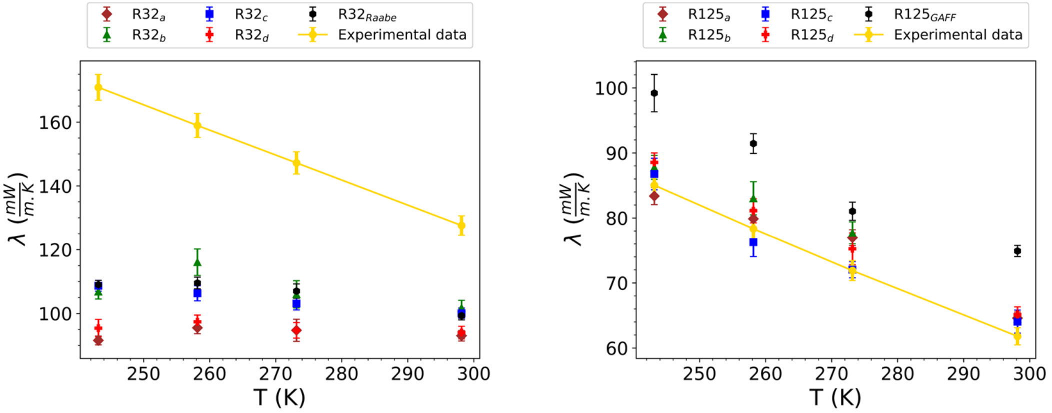

Figure 10. Thermal conductivity as a function of saturation temperature at the corresponding saturation pressure shown in Table 3 for R32 and R125. MAPEs are R32$_a$ = 37.28%, R32$_b$ = **28.18** %, R32$_c$ = 30.26%, R32$_d$ = 36.23%, and R32$_{Raabe}$ = 29.19%; R125$_a$ = 3.88%, R125$_b$ = 5.40%, R125$_c$ = **2.13** %, R125$_d$ = 4.43%, and R125$_{GAFF}$ = 16.83%.

μ_{JT} are extremely sensitive to the accuracy of the α_P values used. α_P values with 10−20% deviation from the experimental value can result in a deviation of close to 100% or even higher depending on the sign of μ_{JT}. The point at which the μ_{JT} curve changes sign from negative to positive is known as the inversion temperature. At this point, μ_{JT} is generally associated with high uncertainties. μ_{JT} has a value of zero at the inversion temperature; thus, any estimate of the percentage absolute deviation from the experimental value at (or near) the inversion temperature tends toward infinity. The very high overall MAPE values in μ_{JT} observed for R125 are due to the extremely high percentage deviation from experimental values close to the inversion temperature. Figure 9 shows that 273.15 K is very close to the inversion temperature. The experimental value of μ_{JT} at 273.15 K is -3.52×10^{-9} K/Pa. The percentage absolute deviations from experiments for R125$_b$, which had the best performance of the R125 FFs for μ_{JT}, are 0.5%, 17.8%, 1112.4%, and 44.3% at 243.15, 258.15, 273.15, and 298.15 K respectively. If the data at 273.15 K (near inversion temperature) is excluded, the MAPE value for R125$_b$ is approximately 21%, which is much lower than 288.31% when this value is included. A MAPE of 21% is quite good considering the sensitivity of the results to the values of α_P. It is interesting to note that R32$_a$ gives a MAPE of 3.48% which is very good. The high accuracy can be attributed to the very low MAPE value of 2.72% in α_P for this particular R32 FF. Overall, it can be concluded that the best MLD-tuned FFs for both R32 and R125 give a decent overall qualitative and quantitative prediction of μ_{JT}.

Thermal Conductivity (λ) and Viscosity (η). Thermal conductivity (λ) and viscosity (η) were computed using nonequilibrium molecular dynamics (NEMD) based methods. These methods require the use of a cuboid-shaped simulation box that is usually longer in one dimension than in the other two. In this work, the final configurations from NPT simulations were used as inputs for a box reshaping run. A 0.5 ns NVT simulation was carried out at the desired ρ and temperature. This was followed by a reshaping of the box to x:y:z dimensions of 3:3:20. These x:y:z dimensions of 3:3:20 are based on the recommendation by Ohara et al.[70] as a way of mitigating box length effects on thermal conductivity results. The deform tool in LAMMPS[44] was used to enforce the box reshaping during a 0.1 ns run in an NVE simulation. To resume the desired simulation temperature, a 5.4 ns NVT simulation was performed using the reshaped simulation box, after which a 4 ns NVE run was performed. The final configuration from this step was used as input for the onward calculation of λ or η in an NVE ensemble using NEMD methods.

Thermal Conductivity. To compute thermal conductivity, we used the heat exchange method proposed by Hafskjold and co-workers.[71,72] The energy exchange was implemented using the enhanced heat exchange (eHEX) algorithm.[73] The energy withdrawal and supply impose a heat flux on the system and drive it away from equilibrium. The system's response results in a temperature gradient in the simulation box from the hot to cold regions. At steady state, this temperature gradient can be related to the magnitude of the external heat flux imposed on the system by Fourier's law of heat conduction to give the thermal conductivity

$$\lambda = -\frac{Q}{\mathrm{d}T/\mathrm{d}z} \tag{17}$$

Q is the imposed heat flux given by

$$Q = \frac{\dot{e}}{A_c} \tag{18}$$

where $\dot{e}$ is the energy exchange rate, which was set to 0.0025 kcal/(mol·fs) in this work and corresponds to 6.95×10^{-6} J/s. A_c is the cross-sectional area of the box.

The simulation box was divided into 20 layers along the z-axis; the two middle layers were defined as the cold region, while the first and last layers at the ends were defined as hot layers with all axes of the simulation box fully periodic. The slope of the linear plot of the temperature profile along the z-axis was used to evaluate dT/dz. The NVE simulations for λ were carried out for 15 ns.

The uncertainties in λ were estimated by using block averaging techniques applied to dT/dz. Preliminary simulations showed that a 6 ns simulation with energy swapping was sufficient to attain a steady state for the value of $\dot{e}$ used. In this work, the last 7.5 ns of the 15 ns simulation was used for further analysis. Calculations of average λ and the associated uncertainties were performed using the instantaneous temperatures in the layers. The uncertainty in λ is a function of the uncertainty in dT/dz as Q is a constant.

Figure 10 shows calculated results of thermal conductivity as a function of saturation temperature at the corresponding

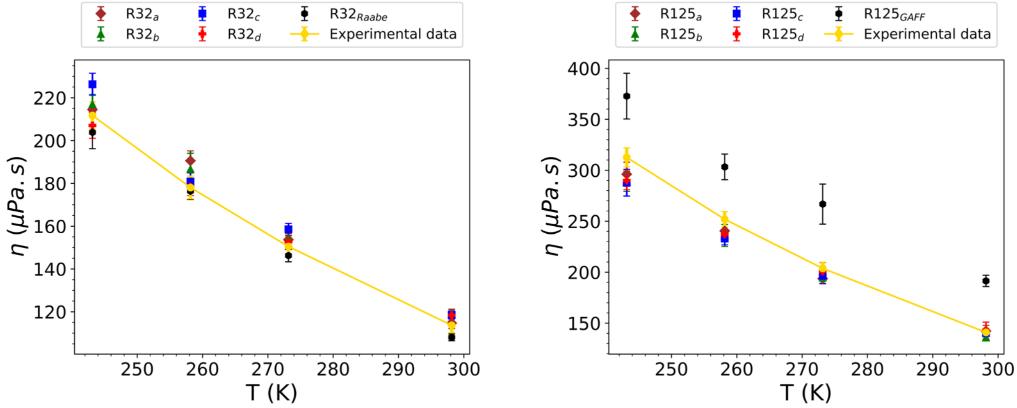

Figure 11. Viscosity as a function of saturation temperature at the corresponding saturation pressure shown in Table 3 for R32 and R125. MAPEs are R32$_a$ = 2.83%, R32$_b$ = 3.66%, R32$_c$ = 4.51%, R32$_d$ = **1.98** %, and R32$_{Raabe}$ = 3.10%; R125$_a$ = **3.90** %, R125$_b$ = 5.47%, R125$_c$ = 4.87%, R125$_d$ = 3.97%, and R125$_{GAFF}$ = 26.62%.

saturation pressure shown in Table 3 for R32 and R125. The experimental data and associated experimental uncertainties used for comparison are the averages of three sets of data for both R32[47,74−77] and R125.[76−78] There is an excellent qualitative and quantitative match between MD simulations and experimental measurements for the MLD-tuned R125 FFs, which clearly outperform the general R125$_{GAFF}$, as can be observed from Figure 10. R125$_c$ gave the best quantitative agreement with a MAPE of 2.14%. The calculated results for R32 show good qualitative agreement but significant quantitative deviations from the experimental measurements. The reason(s) for these discrepancies are not known for certain. We have a hypothesis that there may be some molecular-level mechanisms of heat conduction that these FFs for R32 do not sufficiently capture. One such molecular-level interaction that is worthy of suspicion is weak hydrogen bonding (WHB). R32 is known to demonstrate WHB,[30,79−81] which can be more pronounced than those in some other HFCs that also demonstrate WHB. This hydrogen bonding may have a significant effect on heat conduction at the molecular level.[82,83] Electrostatic and LJ parameters used in classical FFs can be expected to reproduce the hydrogen bonding interactions in molecules; however, there may be a need to apply special treatment to interactions between atomic sites involved in hydrogen bonding[25] to better reproduce certain properties. The reason the R125 FFs are able to predict thermal conductivity values with high accuracy, whereas the R32 FFs do not, may lie with the fact that R125 shows negligible WHB compared to R32. It is worth mentioning, however, that the lowest MAPE value for R32, which is 28.18%, is not too bad since thermal conductivity is generally a challenging transport property to accurately capture.

Viscosity. Viscosity (η) can be reliably computed using an equilibrium molecular dynamics method proposed by Zhang et al.[84] While this is a good approach for computing η and estimating uncertainties, we chose to adopt an NEMD scheme in this work instead. The choice to use NEMD in this work is mainly a matter of convenience. This is because the work performed in preparing the system for a NEMD computation of λ can be leveraged for computing η for the same state points at which λ values were computed. It can be argued that this may be computationally more efficient than having to set up multiple (30 in the original work by Zhang et al.[84]) independent simulations in the canonical ensemble to compute viscosity at a single state point. For the NEMD approach, we only need one additional simulation for a single state point.

There are several NEMD schemes for computing viscosity.[85] The Muller-Plathe method[86] was applied in this work. The method involves imposing an external momentum flux in the simulation box via a momentum swap between two regions of the box. The system's "natural" attempt to counter this imposed momentum flux results in a velocity gradient, which is related to the total imposed momentum flux J to give the fluid viscosity according to

$$\eta = -\frac{J}{\mathrm{d}v/\mathrm{d}z} \tag{19}$$

where dv/dz is the velocity gradient along the z-axis. In this work, momentum swap was performed every 400 fs on the z-components of the momenta of the target atoms, resulting in a velocity gradient along the z-axis. The total imposed momentum flux can be obtained directly from LAMMPS as an output of the "fix viscosity" command and dv/dz is obtained by a linear fit of the velocity profile along the z direction. The uncertainties in η were computed using a similar block averaging method as applied for λ.

The results in Figure 11 show excellent qualitative and quantitative agreement between MD and the experiments for all FFs except R125$_{GAFF}$. R32$_{Raabe}$ compares favorably with the MLD-tuned FFs for R32. The MLD-tuned FFs for R125 clearly outperformed the generalized FF R125$_{GAFF}$. In a previous study, Fouad and Alasiri used a class II FF to calculate the viscosity of R32.[30] Their simulation generally underestimates the experimental values. For example, the values predicted at 243 and 273 K are 195 and 138 μPa·s, respectively, corresponding to an absolute percentage deviation (APD) of 7.9% and 8.3% from experimental values. In the current work, the highest APDs of the MLD-tuned R32 FFs for η are 6.9% and 5.3% at 243.15 and 273.15 K, respectively. The best of the MLD-tuned R32 FF, R32$_a$, gives APDs of 1.3% and 2.1% at 243.15 and 273.15 K respectively.

Self-Diffusivity (*D*). Experimental self-diffusivity data are not available for R32 or R125, and therefore, no comparison can be made between simulation and experiments. However, self-diffusivity was still computed in this work, and the results are reported, as it is considered an important transport property. This will provide data for future MD or experimental work against which to compare.

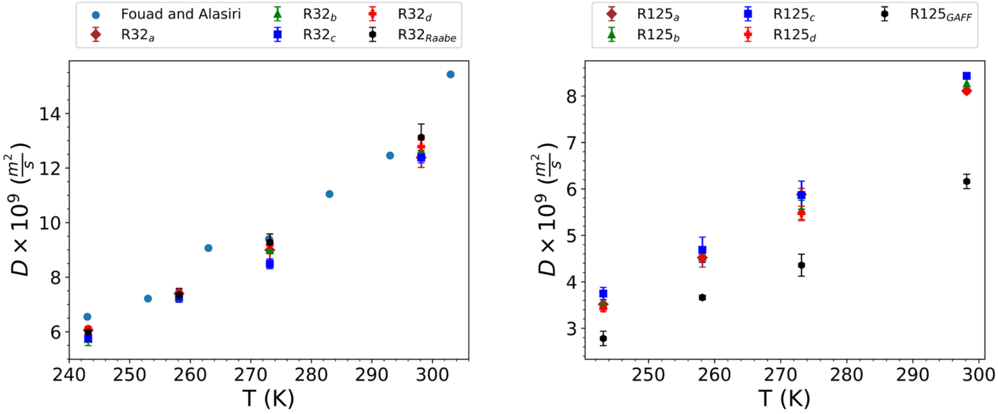

Figure 12. Calculated self-diffusivity as a function of saturation temperature at the corresponding saturation pressure shown in Table 3 for R32 and R125.

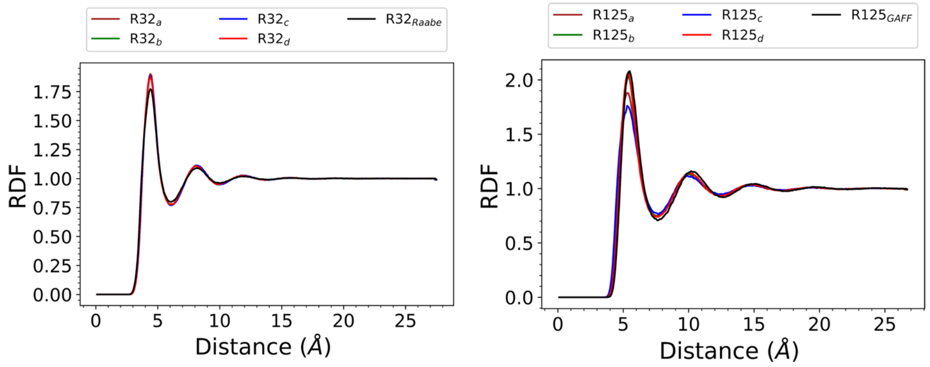

Figure 13. Calculated COM RDFs for R32 and R125 at 273.15 K.

Self-diffusivity is given by the Einstein relation as shown in eq 20.[87]

$$D = \frac{1}{6}\lim_{t\to\infty} \frac{\mathrm{d}}{\mathrm{d}t}\langle[\mathbf{r}(t) - \mathbf{r}(0)]^2\rangle \tag{20}$$

Three independent NVT simulations were used to compute the average D and the uncertainties. The first NVT simulation was carried out for 15 ns after which the velocities were reassigned using a different random seed. A new NVT simulation was then performed for 5 ns. The atomic velocities were reassigned again, and the third independent trajectory was generated. Python LAMMPS Analysis Tools (PyLAT)[88] were used to compute self-diffusivities from these trajectories. The uncertainties in D were estimated as the standard deviation in the independently calculated values of D. System size corrections were applied using Yeh and Hummer's method[89] with the viscosities calculated in this work.

Figure 12 shows the results of D for R32 and R125. MD results by Fouad and Alasiri[30] for R32 are also included. There is generally good qualitative and quantitative agreement between the results from this work and those of Fouad and Alasiri; however, those of Fouad and Alasiri are slightly higher. This is to be expected since the class II FF used in the work by Fouad and Alasiri[30] underestimates the viscosities. It is observed in the current work that the MLD-tuned FFs agree with one another, while R125$_{GAFF}$ predicts lower D values.

Center of Mass (COM) Radial Distribution Function (RDF). PyLAT[88] was used to calculate COM RDFs from the same trajectories used in computing D.

Figure 13 shows that the MLD-tuned FFs for R32 predict very similar liquid structures. R32$_{Raabe}$ predicts the same peak positions as the MLD-tuned FFs but suggests slightly reduced ordering in the first coordination shell in the liquid state at 273.15 K, as shown by the lower peak height. The results for R125 show more pronounced differences in the structural predictions of the MLD-tuned FFs compared to those for R32.

FF Ranking. Tables 5 and 6 compare the results from this work that are relevant to rank the FFs. The first six properties, λ, η, C_P, C_V, α_P, and γ_ρ, are directly simulated properties (DSPs). The other properties, β_T, c_{sound}, and μ_{JT}, were computed indirectly using standard thermodynamic relations involving the relevant DSPs. In each row, the best FF is highlighted in bold.

To ensure a robust parameter recommendation, we considered several different quantitative ranking criteria to identify, if possible, the best force field for each molecule. In our opinion, averaging the MAPEs for all DSPs is the most straightforward approach, as this assigns equal weights to each physical property. Alternately, we can average the MAPEs for all DSPs except λ, which has an order of magnitude larger MAPE compared to the other DSPs for all considered R32 FFs. Yet another ranking criterion is the average MAPE for all properties (directly and indirectly computed), with the exception of μ_{JT}. This can be useful for accessing the performance of FFs studied across more properties in addition to the DSPs while avoiding the overbearing effects of the curious sensitivity of μ_{JT} to α_P. Finally, we considered averaging the MAPEs for all nine properties. The last two criteria were considered less objective for ranking compared

Table 5. Summary of the Performance of the R32 FFs[a]

property	MAPE/(%) **$R32_a$**	$R32_b$	$R32_c$	$R32_d$	$R32_{Raabe}$
λ (DSP, NVE)	37.28	**28.18**	30.26	36.23	29.19
η (DSP, NVE)	2.83	3.66	4.51	**1.98**	3.10
C_P (DSP, NPT)	**5.70**	7.23	8.90	5.87	16.70
C_V (DSP, NVT)	6.92	7.01	6.64	7.13	**4.75**
α_P (DSP, NPT)	**2.72**	17.57	11.42	11.95	14.89
γ_ρ (DSP, NVT)	4.56	**3.21**	5.59	7.24	3.47
β_T	**3.76**	18.16	7.06	14.65	11.12
c_{sound}	4.82	**2.11**	5.88	6.74	3.63
MAPEs for μ_{JT}/(%)	**3.44**	99.80	42.80	58.89	90.00
MAEs for $\mu_{JT} \times 10^8/(K{\cdot}Pa^{-1})$	**0.46**	10.42	5.27	5.88	7.76
normalized MAEs for μ_{JT}	**0.02**	0.50	0.25	0.28	0.37
averaged MAPEs for DSPs except λ/(%)	**4.55**	7.74	7.41	6.84	8.58
averaged MAPEs for all DSPs/(%)	**10.00**	11.14	11.22	11.74	12.02
averaged MAPEs for all properties except μ_{JT}/(%)	**8.57**	10.89	10.03	11.48	10.86
averaged MAPEs for all properties/(%)	**8.00**	20.77	13.67	16.74	19.65
rank based on averaged MAPEs for all DSPs	**1**	2	3	4	5
	MAPEs of VLE properties/(%)[36] **$R32_a$**	$R32_b$	$R32_c$	$R32_d$	$R32_{Raabe}$
ρ^l_{sat}	0.29	0.49	0.27	**0.15**	1.45
ρ^v_{sat}	**1.20**	1.34	1.25	1.23	7.17
P_{vap}	1.03	1.09	**0.53**	1.48	4.30
ΔH_{vap}	0.77	0.63	1.00	**0.45**	2.49
T_c	0.43	0.16	0.40	**0.08**	2.08
ρ_c	0.26	0.49	**0.18**	0.30	0.26
averaged MAPEs for VLE properties	0.66	0.70	**0.60**	0.61	2.96

[a] Minimum per row in bold.

Table 6. Summary of the Performance of the R125 FFs[a]

property	MAPE/(%) $R125_a$	**$R125_b$**	$R125_c$	$R125_d$	$R125_{GAFF}$
λ (DSP, NVE)	3.88	5.40	**2.13**	4.43	16.83
η (DSP, NVE)	**3.90**	5.47	4.87	3.97	26.62
C_P (DSP, NPT)	6.91	7.11	**4.95**	5.27	6.55
C_V (DSP, NVT)	5.13	**3.72**	4.67	4.28	3.79
α_P (DSP, NPT)	10.04	**8.59**	13.61	11.55	31.87
γ_ρ (DSP, NVT)	17.75	**8.02**	15.75	15.03	34.88
β_T	20.75	**15.24**	24.96	21.37	47.57
c_{sound}	14.56	**6.11**	13.80	12.08	36.77
MAPEs for μ_{JT}/(%)	386.26	**288.41**	598.58	523.89	1387.13
MAEs for $\mu_{JT} \times 10^8/(K{\cdot}Pa^{-1})$	6.74	**5.79**	9.73	8.31	20.70
normalized MAEs for μ_{JT}	0.18	**0.15**	0.25	0.22	0.54
averaged MAPEs for DSPs except λ/(%)	8.75	**6.58**	8.77	8.02	20.74
averaged MAPEs for all DSPs/(%)	7.94	**6.39**	7.67	7.42	20.09
averaged MAPEs for all properties except μ_{JT}/(%)	10.36	**7.46**	10.59	9.75	25.61
averaged MAPEs for all properties/(%)	52.13	**38.67**	75.93	66.87	176.89
rank based on averaged MAPEs for all DSPs	4	**1**	3	2	5
	MAPEs of VLE properties/(%)[36] $R125_a$	**$R125_b$**	$R125_c$	$R125_d$	$R125_{GAFF}$
ρ^l_{sat}	1.03	0.69	1.74	**0.40**	2.92
ρ^v_{sat}	2.21	1.60	**1.00**	2.47	50.52
P_{vap}	2.20	**1.76**	1.99	2.42	46.05
ΔH_{vap}	1.42	2.47	**0.93**	2.39	22.37
T_c	1.08	0.71	**0.63**	0.91	9.02
ρ_c	0.83	0.77	1.57	**0.17**	8.48
averaged MAPEs for VLE properties	1.46	1.33	**1.31**	1.46	23.23

[a] Minimum per row in bold.

with the criterion of averaging MAPEs for all DSPs only. This is because using the last two criteria may lead to an overweighting of the effects of some of the DSPs such as α_P.

Interestingly, we find that all four ranking criteria recommend the same best FFs: $R32_a$ and $R125_b$. This outcome is not guaranteed, and we do not expect it to hold universally that all four ranking criteria will always suggest the same "best" FF. We also observe that all four ranking criteria give different orders besides the top rank, e.g., rank 2 and rank 3. For comparison, the MAPE results for VLE properties used by Befort et al.[36] to rank the force fields are reported at the bottom of Tables 5 and 6.

The MAPEs for μ_{JT} in Tables 5 and 6 suggest at first glance that the MLD-tuned FFs for R125 perform significantly worse at capturing μ_{JT} than the R32 FFs. However, such a conclusion may be misleading. To enable a better quantitative assessment of the performance of the FFs for predicting μ_{JT}, the mean absolute errors (MAEs) and normalized MAEs for μ_{JT} are included in Tables 5 and 6. The MAEs are normalized using the maximum absolute values of the corresponding experimental data for R32 and R125, within the temperature range of interest. The comparison of the MAEs and normalized MAEs of the MLD-tuned FFs for R32 and R125 in Tables 5 and 6 shows that the R125 FFs are not much worse than the R32 FFs in predicting μ_{JT}. The MAE values are, in general, very low. Three of the four MLD-tuned FFs for R32 and all of the MLD-tuned R125 FFs have MAE values ranging between $5{-}10 \times 10^{-8}/(K{\cdot}Pa^{-1})$ showing that the performances of the FFs for R125 are in general comparable to those of the R32 FFs. The normalized MAE values are generally less than 0.3 for most of the MLD-tuned FFs for R32 and R125. This can be considered a decent value considering the sensitivity of μ_{JT} to α_P. This further addresses the issue of the poor predictive performance of R125 FFs for μ_{JT} that may arise by focusing on only MAPE values.

The MLD-tuned FFs generally demonstrate excellent transferability across all of the properties investigated at multiple state points. They perform better than the expert-tuned FF for R32 and the generalized FF for R125. We consider it remarkable that the MLD-tuned FFs are transferable to a wide range of properties not used in tuning them. There is no simple or direct correlation between the properties used for tuning and some of the captured properties, like transport properties for example. Furthermore, only the LJ parameters were tuned for these MLD-tuned FFs using bonded parameters from one of the early GAFF versions, which used relatively less expensive quantum calculations for obtaining the bonded parameters. Our results suggest that, for the purposes of capturing thermophysical and transport properties of simple fluids like HFCs, we do not always have to tune bonded parameters to very high accuracy, decent is good enough. We consider this to be remarkable. Finally, we find it somewhat surprising that MLD-tuning was able to obtain not one but several FF parameter sets that outperform expert-tuned FFs in terms of transferability to other properties. The qualities and performances of these MLD-tuned FFs for VLE properties are generally transferred to the other properties computed in this work, further confirming that these MLD-tuned FFs capture to a good extent the actual physics of the molecules they have been designed to represent.

The extensive and rigorous evaluation of MLD-tuned FFs using various properties that were not involved in tuning them can help to better distinguish and rank FFs that were nearly indistinguishable solely on the basis of VLE properties. The range of the average MAPE for VLE properties is 0.1% and 0.15% for MLD-tuned R32 and R125 FFs, respectively, whereas, for the DSPs studied in this work, we obtain a range of 1.73% and 1.54% for R32 and R125, respectively. This is more than an order of magnitude higher than that in the VLE properties. When derivative properties, such as α_P and γ_ρ, are also considered, for which significant differences were observed between the FFs, we can confidently conclude that these MLD-tuned FFs, though similar in performance for several properties, are indeed different and may not always tell the same story.

From Tables 5 and 6, we see that the FF parameter sets that give the lowest MAPE values for multiple VLE properties do not necessarily provide the best generalizability to several other properties. For both R32 and R125, the FFs with the lowest average MAPE based on VLE results, which may have been considered the best FFs in our prior work,[36] were not the best FF parameter sets for the physical properties examined in this study. One interpretation is that the FFs optimized only for VLE properties, i.e., top FF from Befort et al.,[36] are overfit and thus have relatively higher errors for properties not used for calibration. This is consistent with common knowledge in statistics, data science, and machine learning about overfitting and the bias-variance trade-off.

We may speculate from Tables 5 and 6 that inputting liquid densities outside saturation conditions as a property for tuning FFs in addition to the VLE properties used by Befort et al.[36] may lead to a significant improvement in the transferability of these MLD-tuned FFs to other thermodynamic properties. For example, predicting α_P for the saturated liquid state using finite-difference methods requires highly accurate liquid densities not just at saturation conditions but also at conditions outside saturation conditions. Therefore, including liquid densities outside saturation conditions for training FFs may be important for a better performance of MLD-tuned FFs for predicting volumetric thermodynamic properties. This will in turn lead to more accurate indirectly computed thermodynamic properties.

CONCLUSIONS

This work has demonstrated that MLD-tuned FFs developed previously based on VLE properties are transferable to a wider range of thermophysical and transport properties not used in the tuning procedure. We have also found that the similarities observed in performance in the VLE properties are also observed across other properties but to a significantly lower degree, such that we can begin to distinguish between these FFs by calculating properties not used in tuning the FFs parameters. Based on the properties studied in this work, we identified R32$_a$ and R125$_b$ as the overall best and therefore recommend them for future simulations.

This paper provides an extensive set of simulation data on a wide range of thermophysical, transport, and structural properties for two important refrigerants. The results and corresponding postprocessing tools should be helpful to others wishing to perform simulations on similar or other systems.

ASSOCIATED CONTENT

Data Availability Statement

Calculated properties, sample input scripts, and postprocessing codes used in this work are available to the public on the project's Open Science Framework and GitHub repository at https://osf.io/t9265/ and https://github.com/MaginnGroup/Validation-of-HFC-FFs, respectively.

Supporting Information

The Supporting Information is available free of charge at https://pubs.acs.org/doi/10.1021/acs.jced.3c00379.

Additional simulation details, uncertainty quantification methods, and all tabulated results (PDF)

AUTHOR INFORMATION

Corresponding Author

Edward J. Maginn − *Department of Chemical and Biomolecular Engineering, University of Notre Dame, Notre Dame, Indiana 46556, United States;* orcid.org/0000-0002-6309-1347; Email: ed@nd.edu

Authors

Barnabas Agbodekhe − *Department of Chemical and Biomolecular Engineering, University of Notre Dame, Notre Dame, Indiana 46556, United States;* orcid.org/0000-0001-6293-4296

Eliseo Marin-Rimoldi − *Department of Chemical and Biomolecular Engineering, University of Notre Dame, Notre Dame, Indiana 46556, United States*

Yong Zhang − *Department of Chemical and Biomolecular Engineering, University of Notre Dame, Notre Dame, Indiana 46556, United States;* orcid.org/0000-0003-3988-5961

Alexander W. Dowling − *Department of Chemical and Biomolecular Engineering, University of Notre Dame, Notre Dame, Indiana 46556, United States;* orcid.org/0000-0001-9383-7499

Complete contact information is available at: https://pubs.acs.org/10.1021/acs.jced.3c00379

Notes

The authors declare no competing financial interest.

ACKNOWLEDGMENTS

The authors acknowledge funding from the National Science Foundation (NSF) EFRI DChem: Next-generation Low Global Warming Refrigerants, Award no. 2029354, and CBET Development and Application of a Molecular and Process Design Framework for the Separation of Hydrofluorocarbon Mixtures, Award no. 1917474. Computational resources were provided by the Center for Research Computing (CRC) at the University of Notre Dame.

■ REFERENCES

(1) United Nations. About Montreal Protocol; 2018; https://www.unep.org/ozonaction/who-we-are/about-montreal-protocol.

(2) United Nations. GWP-ODP Calculator; 2018; https://www.unep.org/ozonaction/gwp-odp-calculator.

(3) Department of Ecology, State of Washington. Hydrofluorocarbon transition; 2023; https://ecology.wa.gov/Air-Climate/Reducing-Emissions/Hydrofluorocarbons.

(4) U.S. EPA. Reducing Hydrofluorocarbon (HFC) Use and Emissions in the Federal Sector through SNAP; 2014; https://www.epa.gov/snap/reducing-hydrofluorocarbon-hfc-use-and-emissions-federal-sector-through-snap.

(5) Davenport, C. Nations, Fighting Powerful Refrigerant That Warms Planet, Reach Landmark Deal. *The New York Times* 2016.

(6) McGrath, M. Climate Change: 'Monumental' Deal to Cut HFCs, Fastest Growing Greenhouse Gases. *BBC News*, 2016.

(7) Velders, G. J. M.; Fahey, D. W.; Daniel, J. S.; McFarland, M.; Andersen, S. O. The Large Contribution of Projected HFC Emissions to Future Climate Forcing. *Proc. Natl. Acad. Sci. U. S. A.* **2009**, *106*, 10949−10954.

(8) McLinden, M. O.; Brown, J. S.; Brignoli, R.; Kazakov, A. F.; Domanski, P. A. Limited Options for Low-Global-Warming-Potential Refrigerants. *Nat. Commun.* **2017**, *8*, 14476.

(9) Alkhatib, I. I. I.; Albà, C. G.; Darwish, A. S.; Llovell, F.; Vega, L. F. Searching for Sustainable Refrigerants by Bridging Molecular Modeling with Machine Learning. *Ind. Eng. Chem. Res.* **2022**, *61*, 7414−7429.

(10) Tillner-Roth, R.; Yokozeki, A. An International Standard Equation of State for Difluoromethane (R-32) for Temperatures from the Triple Point at 136.34 to 435 K and Pressures up to 70 MPa. *J. Phys. Chem. Ref. Data* **1997**, *26*, 1273−1328.

(11) Lemmon, E. W.; Jacobsen, R. T. A New Functional Form and New Fitting Techniques for Equations of State with Application to Pentafluoroethane (HFC-125). *J. Phys. Chem. Ref. Data* **2005**, *34*, 69−108.

(12) Sobati, M. A.; Abooali, D. Molecular Based Models for Estimation of Critical Properties of Pure Refrigerants: Quantitative Structure Property Relationship (QSPR) Approach. *Thermochim. Acta* **2015**, *602*, 53−62.

(13) Abooali, D.; Sobati, M. A. Novel Method for Prediction of Normal Boiling Point and Enthalpy of Vaporization at Normal Boiling Point of Pure Refrigerants: A QSPR Approach. *Int. J. Refrig* **2014**, *40*, 282−293.

(14) Godavarthy, S. S.; Robinson, R. L.; Gasem, K. A. M. Improved Structure−Property Relationship Models for Prediction of Critical Properties. *Fluid Ph. Equilibria* **2008**, *264*, 122−136.

(15) Morais, A. R. C.; Harders, A. N.; Baca, K. R.; Olsen, G. M.; Befort, B. J.; Dowling, A. W.; Maginn, E. J.; Shiflett, M. B. Phase equilibria, diffusivities, and equation of state modeling of HFC-32 and HFC-125 in imidazolium-based ionic liquids for the separation of R-410A. *Ind. Eng. Chem. Res.* **2020**, *59*, 18222−18235.

(16) Baca, K. R.; Olsen, G. M.; Matamoros Valenciano, L.; Bennett, M. G.; Haggard, D. M.; Befort, B. J.; Garciadiego, A.; Dowling, A. W.; Maginn, E. J.; Shiflett, M. B. Phase Equilibria and Diffusivities of HFC-32 and HFC-125 in Ionic Liquids for the Separation of R-410A. *ACS Sustain. Chem. Eng.* **2022**, *10*, 816−830.

(17) Garciadiego, A.; Befort, B. J.; Franco, G.; Mazumder, M.; Dowling, A. W. What data are most valuable to screen ionic liquid entrainers for hydrofluorocarbon refrigerant reuse and recycling? *Ind. Eng. Chem. Res.* **2022**, *61*, 18412.

(18) Befort, B. J.; Garciadiego, A.; Wang, J.; Wang, K.; Franco, G.; Maginn, E. J.; Dowling, A. W. Data science for thermodynamic modeling: Case study for ionic liquid and hydrofluorocarbon refrigerant mixtures. *Fluid Ph. Equilibria* **2023**, *572*, 113833.

(19) Monjur, M. S.; Iftakher, A.; Hasan, M. F. Separation process synthesis for high-GWP refrigerant mixtures: Extractive distillation using ionic liquids. *Ind. Eng. Chem. Res.* **2022**, *61*, 4390−4406.

(20) Asensio-Delgado, S.; Pardo, F.; Zarca, G.; Urtiaga, A. Enhanced absorption separation of hydrofluorocarbon/hydrofluoroolefin refrigerant blends using ionic liquids. *Sep. Purif. Technol.* **2020**, *249*, 117136.

(21) Finberg, E. A.; Shiflett, M. B. Process designs for separating R-410A, R-404A, and R- 407C using extractive distillation and ionic liquid entrainers. *Ind. Eng. Chem. Res.* **2021**, *60*, 16054−16067.

(22) Albá, C. G.; Alkhatib, I. I.; Llovell, F.; Vega, L. F. Assessment of low global warming potential refrigerants for drop-in replacement by connecting their molecular features to their performance. *ACS Sustain. Chem. Eng.* **2021**, *9*, 17034−17048.

(23) Garciadiego, A.; Mazumder, M.; Befort, B. J.; Dowling, A. W. *Computer Aided Chemical Engineering*; Elsevier, 2022; Vol. *49*, pp 307−312;.

(24) Hwang, M. J.; Stockfisch, T. P.; Hagler, A. T. Derivation of Class II Force Fields. 2. Derivation and Characterization of a Class II Force Field, CFF93, for the Alkyl Functional Group and Alkane Molecules. *J. Am. Chem. Soc.* **1994**, *116*, 2515−2525.

(25) Leach, A. *Molecular Modelling Principles and Applications*, 2nd ed.; Pearson Education Limited: Essex, England, 2001.

(26) Sun, H. COMPASS: An Ab Initio Force-Field Optimized for Condensed-Phase ApplicationsOverview with Details on Alkane and Benzene Compounds. *J. Phys. Chem. B* **1998**, *102*, 7338−7364.

(27) Sun, H.; Jin, Z.; Yang, C.; Akkermans, R. L. C.; Robertson, S. H.; Spenley, N. A.; Miller, S.; Todd, S. M. COMPASS II: Extended Coverage for Polymer and Drug-like Molecule Databases. *J. Mol. Model* **2016**, *22*, 47.

(28) Yu, W.; Liu, C.; Li, Q.; Xin, L.; Wang, S. Resource Utilization of Waste HFC-134a Refrigerant by Supercritical Gasification Method: A Reactive Molecular Dynamic Study. *Process Saf. Environ. Prot.* **2022**, *168*, 399−409.

(29) Alam, M. S.; Jeong, J. H. Comparative Molecular Dynamics Simulations of Homogeneous Condensation of Refrigerants. *Int. J. Therm. Sci.* **2019**, *141*, 187−198.

(30) Fouad, W. A.; Alasiri, H. Molecular Dynamic Simulation and SAFT Modeling of the Viscosity and Self-Diffusion Coefficient of Low Global Warming Potential Refrigerants. *J. Mol. Liq.* **2020**, *317*, 113998.

(31) Jaramillo, E.; Grey, C. P.; Auerbach, S. M. Molecular Dynamics Studies of Hydrofluorocarbons in Faujasite-type Zeolites: Modeling Guest-Induced Cation Migration in Dry Zeolites. *J. Phys. Chem. B* **2001**, *105*, 12319−12329.

(32) Khan, M.; Wen, J.; Shakoori, M. A.; Tao, W. Homogeneous Condensation and Ther mophysical Properties of R450A, R513A and R515A Using Molecular Dynamics Simulations. *J. Mol. Liq.* **2022**, *353*, 118795.

(33) Stephan, S.; Horsch, M. T.; Vrabec, J.; Hasse, H. MolMod − an Open Access Database of Force Fields for Molecular Simulations of Fluids. *Mol. Simul.* **2019**, *45*, 806−814.

(34) Wang, J.; Wolf, R. M.; Caldwell, J. W.; Kollman, P. A.; Case, D. A. Development and Testing of a General Amber Force Field. *J. Comput. Chem.* **2004**, *25*, 1157−1174.

(35) Jorgensen, W. L.; Maxwell, D. S.; Tirado-Rives, J. Development and Testing of the OPLS All-Atom Force Field on Conformational Energetics and Properties of Organic Liquids. *J. Am. Chem. Soc.* **1996**, *118*, 11225−11236.

(36) Befort, B. J.; DeFever, R. S.; Tow, G. M.; Dowling, A. W.; Maginn, E. J. Machine Learning Directed Optimization of Classical Molecular Modeling Force Fields. *J. Chem. Inf. Model.* **2021**, *61*, 4400−4414.

(37) Raabe, G. Molecular Simulation Studies on the Vapor−Liquid Phase Equilibria of Binary Mixtures of R-1234yf and R-1234ze(E) with R-32 and CO $_2$. *J. Chem. Eng. Data* **2013**, *58*, 1867−1873.

(38) Fermeglia, M.; Ferrone, M.; Pricl, S. Development of an All-Atoms Force Field from Ab Initio Calculations for Alternative Refrigerants. *Fluid Ph. Equilibria* **2003**, *210*, 105−116.

(39) Wang, N.; Carlozo, M. N.; Marin-Rimoldi, E.; Befort, B. J.; Dowling, A. W.; Maginn, E. J. Machine Learning-Enabled Development of Accurate Force Fields for Refrigerants. *J. Chem. Theory Comput.* **2023**, *19*, 4546.

https://doi.org/10.1021/acs.jced.3c00379
J. Chem. Eng. Data XXXX, XXX, XXX−XXX

(40) Peguin, R. P. S.; Kamath, G.; Potoff, J. J.; da Rocha, S. R. P. All-Atom Force Field for the Prediction of Vapor-Liquid Equilibria and Interfacial Properties of HFA134a. *J. Phys. Chem. B* **2009**, *113*, 178−187.

(41) Yang, Z.; Gong, M.; Dong, X.; Li, X.; Wu, J. Molecular Modeling and Simulation of Vapor−Liquid Equilibrium of the Refrigerant R152a and Its Mixture R152a+R32. *Fluid Ph. Equilibria* **2015**, *394*, 93−100.

(42) Zhang, N.; Hu, P.; Chen, L.; Zhi, L. Molecular Modeling of Vapor-Liquid Equilibrium Properties of HFC-161 and Its Mixture HFC-161+HFO-1234yf. *J. Mol. Liq.* **2020**, *306*, 112896.

(43) Bayly, C. I.; Cieplak, P.; Cornell, W.; Kollman, P. A. A Well-Behaved Electrostatic Potential Based Method Using Charge Restraints for Deriving Atomic Charges: The RESP Model. *J. Phys. Chem.* **1993**, *97*, 10269−10280.

(44) Thompson, A. P.; Aktulga, H. M.; Berger, R.; Bolintineanu, D. S.; Brown, W. M.; Crozier, P. S.; in 't Veld, P. J.; Kohlmeyer, A.; Moore, S. G.; Nguyen, T. D.; et al. LAMMPS - a Flexible Simulation Tool for Particle-Based Materials Modeling at the Atomic, Meso, and Continuum Scales. *Comput. Phys. Commun.* **2022**, *271*, 108171.

(45) Martínez, J. M.; Martínez, L. Packing Optimization for Automated Generation of Complex System's Initial Configurations for Molecular Dynamics and Docking. *J. Comput. Chem.* **2003**, *24*, 819−825.

(46) Martínez, L.; Andrade, R.; Birgin, E. G.; Martínez, J. M. PACKMOL: A Package for Building Initial Configurations for Molecular Dynamics Simulations. *J. Comput. Chem.* **2009**, *30*, 2157−2164.

(47) Huber, M. L.; Lemmon, E. W.; Bell, I. H.; McLinden, M. O. The NIST REFPROP Database for Highly Accurate Properties of Industrially Important Fluids. *Ind. Eng. Chem. Res.* **2022**, *61*, 15449−15472.

(48) Ewald, P. P. Die Berechnung optischer und elektrostatischer Gitterpotentiale. *Ann. Phys.* **1921**, *369*, 253−287.

(49) Kolafa, J.; Perram, J. W. Cutoff Errors in the Ewald Summation Formulae for Point Charge Systems. *Mol. Simul.* **1992**, *9*, 351−368.

(50) Lorentz, H.; Berthelot, A. *Lessons on the Theory of the Brownian Movement*; Springer, 1910; pp 261−301.

(51) Shinoda, W.; Shiga, M.; Mikami, M. Rapid Estimation of Elastic Constants by Molecular Dynamics Simulation under Constant Stress. *Phys. Rev. B* **2004**, *69*, 134103.

(52) Tuckerman, M. E.; Alejandre, J.; López-Rendón, R.; Jochim, A. L.; Martyna, G. J. A Liouville-operator Derived Measure-Preserving Integrator for Molecular Dynamics Simulations in the Isothermal−Isobaric Ensemble. *J. Phys. A: Math. Gen.* **2006**, *39*, 5629.

(53) Flyvbjerg, H.; Petersen, H. G. Error Estimates on Averages of Correlated Data. *J. Chem. Phys.* **1989**, *91*, 461−466.

(54) Frenkel, D.; Smit, B. *Understanding Molecular Simulation: From Algorithms to Applications*, 1st ed.; Academic Press, Inc.: New York, USA, 1996.

(55) Virtanen, P.; Gommers, R.; Oliphant, T. E.; Haberland, M.; Reddy, T.; Cournapeau, D.; Burovski, E.; Peterson, P.; Weckesser, W.; Bright, J.; et al. SciPy 1.0: Fundamental Algorithms for Scientific Computing in Python. *Nat. Methods* **2020**, *17*, 261−272.

(56) Cadena, C.; Zhao, Q.; Snurr, R. Q.; Maginn, E. J. Molecular Modeling and Experimental Studies of the Thermodynamic and Transport Properties of Pyridinium-Based Ionic Liquids. *J. Phys. Chem. B* **2006**, *110*, 2821−2832.

(57) Lucas, K.; Delfs, U.; Buss, V.; Speis, M. Ideal-Gas Properties of New Refrigerants from Quantum Mechanical Ab Initio Calculations. *Int. J. Thermophys* **1993**, *14*, 993−1006.

(58) Smith, D. G. A.; Burns, L. A.; Simmonett, A. C.; Parrish, R. M.; Schieber, M. C.; Galvelis, R.; Kraus, P.; Kruse, H.; Di Remigio, R.; Alenaizan, A.; et al. Psi4 1.4: Open source Software for High-Throughput Quantum Chemistry. *J. Chem. Phys.* **2020**, *152*, 184108.

(59) Aimoli, C. G.; Maginn, E. J.; Abreu, C. R. Force Field Comparison and Thermodynamic Property Calculation of Supercritical CO2 and CH4 Using Molecular Dynamics Simulations. *Fluid Ph. Equilibria* **2014**, *368*, 80−90.

(60) Raabe, G. Molecular Simulation Studies on the Thermophysical Properties of the Refrigerant Blend R-445A. *J. Chem. Eng. Data* **2013**, *58*, 3470−3476.

(61) Raabe, G. *Molecular Simulation Studies on Thermophysical Properties*; Molecular Modeling and Simulation; Springer Singapore: Singapore, 2017.

(62) Wang, N.; Zhang, Y.; Maginn, E. J. Molecular Dynamics Study of the Ionic Liquid 1-n-Hexyl-3-Methylimidazolium Tris-(Pentafluoroethyl)Trifluorophosphate ([C6C1im][FAP]): Force Field Development and the Effect of [FAP]- Isomer Content on Properties. *J. Ion. Liq.* **2022**, *2*, 100040.

(63) Wu, Y.; Tepper, H. L.; Voth, G. A. Flexible Simple Point-Charge Water Model with Improved Liquid-State Properties. *J. Chem. Phys.* **2006**, *124*, No. 024503.

(64) Liu, H.; Mueller-Plathe, F.; Van Gunsteren, W. F. A Force Field for Liquid Dimethyl Sulfoxide and Physical Properties of Liquid Dimethyl Sulfoxide Calculated Using Molecular Dynamics Simulation. *J. Am. Chem. Soc.* **1995**, *117*, 4363−4366.

(65) Bordat, P.; Sacristan, J.; Reith, D.; Girard, S.; Glättli, A.; Müller-Plathe, F. An Improved Dimethyl Sulfoxide Force Field for Molecular Dynamics Simulations. *Chem. Phys. Lett.* **2003**, *374*, 201−205.

(66) Ke, Q.; Gong, X.; Liao, S.; Duan, C.; Li, L. Effects of Thermostats/Barostats on Physical Properties of Liquids by Molecular Dynamics Simulations. *J. Mol. Liq.* **2022**, *365*, 120116.

(67) Lagache, M.; Ungerer, P.; Boutin, A.; Fuchs, A. H. Prediction of Thermodynamic Derivative Properties of Fluids by Monte Carlo Simulation. *Phys. Chem. Chem. Phys.* **2001**, *3*, 4333−4339.

(68) Honorio, T. Thermal Conductivity, Heat Capacity and Thermal Expansion of Ettringite and Metaettringite: Effects of the Relative Humidity and Temperature. *Cem. Concr. Res.* **2022**, *159*, 106865.

(69) Alkhwaji, A.; Elbahloul, S.; Abdullah, M. Z.; Bakar, K. F. B. A. Selected Water Thermal Properties from Molecular Dynamics for Engineering Purposes. *J. Mol. Liq.* **2021**, *324*, 114703.

(70) Ohara, T.; Chia Yuan, T.; Torii, D.; Kikugawa, G.; Kosugi, N. Heat Conduction in Chain Polymer Liquids: Molecular Dynamics Study on the Contributions of Inter- and Intramolecular Energy Transfer. *J. Chem. Phys.* **2011**, *135*, No. 034507.

(71) Hafskjold, B.; Ikeshoji, T.; Ratkje, S. K. On the Molecular Mechanism of Thermal Diffusion in Liquids. *Mol. Phys.* **1993**, *80*, 1389−1412.

(72) Ikeshoji, T.; Hafskjold, B. Non-Equilibrium Molecular Dynamics Calculation of Heat Conduction in Liquid and through Liquid-Gas Interface. *Mol. Phys.* **1994**, *81*, 251−261.

(73) Wirnsberger, P.; Frenkel, D.; Dellago, C. An Enhanced Version of the Heat Exchange Algorithm with Excellent Energy Conservation Properties. *J. Chem. Phys.* **2015**, *143*, 124104.

(74) Ro, S. T.; Kim, J. Y.; Kim, D. S. Thermal Conductivity of R32 and Its Mixture with R134a. *Int. J. Thermophys* **1995**, *16*, 1193.

(75) Marsh, K. N.; Perkins, R. A.; Ramires, M. L. Measurement and Correlation of the Thermal Conductivity of Propane From 86 to 600 K at Pressures to 70 MPa. *J. Chem. Eng. Data* **2002**, *47*, 932.

(76) Papadaki, M.; Wakeham, W. A. Thermal Conductivity of R32 and R125 in the Liquid Phase at the Saturation Vapor Pressure. *Int. J. Thermophys* **1993**, *14*, 1215−1220.

(77) Gross, U.; Song, Y. W.; Hahne, E. Thermal Conductivity of the New Refrigerants R134a, R152a, and R123 Measured by the Transient Hot-Wire Method. *Int. J. Thermophys* **1992**, *13*, 957−983.

(78) Perkins, R. A.; Huber, M. L. Measurement and Correlation of the Thermal Conductivity of Pentafluoroethane (R125) from 190 to 512 K at Pressures to 70 MPa. *J. Chem. Eng. Data* **2006**, *51*, 898−904.

(79) Prampolini, G.; Carbonaro, L.; Feng, G.; Evangelisti, L.; Caminati, W.; Cacelli, I. Computational Screening of Weak Hydrogen Bond Networks: Predicting Stable Structures for Difluoromethane Oligomers. *J. Chem. Theory Comput.* **2014**, *10*, 2204−2211.

(80) Almásy, L.; Bende, A. Intermolecular Interaction in Methylene Halide (CH2F2, CH2Cl2, CH2Br2 and CH2I2) Dimers. *Molecules* **2019**, *24*, 1810.

(81) Feng, G.; Evangelisti, L.; Cacelli, I.; Carbonaro, L.; Prampolini, G.; Caminati, W. Oligomers Based on Weak Hydrogen Bond Networks: A Rotational Study of the Tetramer of Difluoromethane. *Chem. Commun.* **2014**, *50*, 171−173.

(82) He, J. Molecular Mechanisms and Design of Hydrogen-Bonded Materials for Thermal Applications. Ph.D. thesis, Utah State University, 2020.

(83) Zhou, J.; Lin, S.; Zeng, H.; Liu, J.; Li, B.; Xu, Y.; Zhao, X.; Chen, G. Dynamic Intermolecular Interactions through Hydrogen Bonding of Water Promote Heat Conduction in Hydrogels. *Mater. Horiz.* **2020**, *7*, 2936−2943.

(84) Zhang, Y.; Otani, A.; Maginn, E. J. Reliable Viscosity Calculation from Equilibrium Molecular Dynamics Simulations: A Time Decomposition Method. *J. Chem. Theory Comput.* **2015**, *11*, 3537−3546.

(85) Tenney, C. M.; Maginn, E. J. Limitations and Recommendations for the Calculation of Shear Viscosity Using Reverse Nonequilibrium Molecular Dynamics. *J. Chem. Phys.* **2010**, *132*, No. 014103.

(86) Müller-Plathe, F. Reversing the Perturbation in Nonequilibrium Molecular Dynamics: An Easy Way to Calculate the Shear Viscosity of Fluids. *Phys. Rev. E* **1999**, *59*, 4894−4898.

(87) Allen, M. P.; Tildesley, D. J. *Computer Simulation of Liquids*, second ed.; Oxford University Press: Oxford, United Kingdom, 2017.

(88) Humbert, M. T.; Zhang, Y.; Maginn, E. J. PyLAT: Python LAMMPS Analysis Tools. *J. Chem. Inf. Model.* **2019**, *59*, 1301−1305.

(89) Yeh, I.-C.; Hummer, G. System-Size Dependence of Diffusion Coefficients and Viscosities from Molecular Dynamics Simulations with Periodic Boundary Conditions. *J. Phys. Chem. B* **2004**, *108*, 15873−15879.

https://doi.org/10.1021/acs.jced.3c00379